THE JOURNAL OF PHYSICAL CHEMISTRY B

pubs.acs.org/JPCB Article

Molecular Mechanism for Azeotrope Formation in Ethanol/Benzene Binary Mixtures through Gibbs Ensemble Monte Carlo Simulation

Dongyang Li, Ziqi Gao, Naveen Kumar Vasudevan, Hong Li, Xin Gao,* Xingang Li, and Li Xi*

Cite This: J. Phys. Chem. B 2020, 124, 3371−3386 Read Online

ABSTRACT: Azeotropes have been studied for decades due to the challenges they impose on separation processes but fundamental understanding at the molecular level remains limited. Although molecular simulation has demonstrated its capability of predicting mixture vapor−liquid equilibrium (VLE) behaviors, including azeotropes, its potential for mechanistic investigation has not been fully exploited. In this study, we use the united atom transferable potentials for phase equilibria (TraPPE-UA) force field to model the ethanol/benzene mixture, which displays a positive azeotrope. Gibbs ensemble Monte Carlo (GEMC) simulation is performed to predict the VLE phase diagram, including an azeotrope point. The results accurately agree with experimental measurements. We argue that the molecular mechanism of azeotrope formation cannot be fully understood by studying the mixture liquid-state stability at the azeotrope point alone. Rather, azeotrope occurrence is only a reflection of the changing relative volatility between the two components over a much wider composition range. A thermodynamic criterion is thus proposed on the basis of the comparison of partial excess Gibbs energy between the components. In the ethanol/benzene system, molecular energetics shows that with increasing ethanol mole fraction, its volatility initially decreases but later plateaus, while benzene volatility is initially nearly constant and only starts to decrease when its mole fraction is low. Analysis of the mixture liquid structure, including a detailed investigation of ethanol hydrogen-bonding configurations at different composition levels, reveals the underlying molecular mechanism for the changing volatilities responsible for the azeotrope.

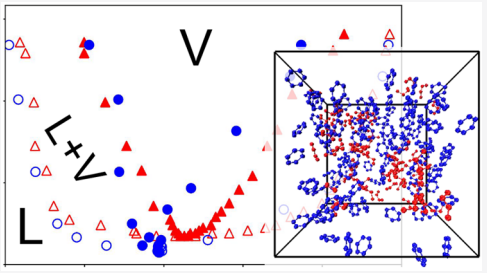

1. INTRODUCTION

Azeotropes are vapor−liquid equilibrium (VLE) states where the compositions are the same between the two coexisting phases, i.e.,

$$x_i = y_i \tag{1}$$

where x_i and y_i are, respectively, the liquid- and vapor-phase mole fractions of component i. Azeotropes are caused by strong deviation from the ideal-mixture behavior (described by the Raoult's law) and their existence poses great challenges for separation processes. Ideal or nearly ideal mixtures can be clearly differentiated according to their volatility on the basis of which separation can be efficiently achieved at VLE states using distillation. However, this no longer applies to azeotropes where volatilities of components are the same. Designing a separation process for azeotropes always begins with VLE data and a phase diagram, which can be obtained by experiments[1−3] or thermodynamic models (excess Gibbs free energy (G^E) models,[4,5] equations of state (EoSs),[6,7] group contribution methods,[8,9] etc.). Experiments become difficult in many circumstances, such as when toxic chemicals or high pressures are involved, and are commonly time-consuming and costly. Existing models are typically constructed by empirical or semiempirical approaches and apply only to specific groups of compounds sharing similar chemical structures. The lack of generality of those models reflects our limited understanding of the molecular origin of the azeotrope phenomenon. Beyond prediction, identifying the molecular interactions responsible for azeotropes can also help us better design their separation processes, e.g., through more guided selection of entrainers used in azeotropic distillation.

In a strictly ideal mixture, the intermolecular interactions between unlike molecules equal those between molecules of the same species and the equilibrium vapor pressure follow the Raoult's law, which a for binary mixture is

$$P = x_1 P_1^{\mathrm{sat}}(T) + x_2 P_2^{\mathrm{sat}}(T) \tag{2}$$

(P_i^{sat} is the vapor pressure of pure species i). An azeotrope occurs when strong deviation from Raoult's law results in a local minimum or maximum in the vapor pressure versus mole fraction curve at constant temperature. A vapor pressure minimum is called a negative or maximum boiling azeotrope,

Received: December 30, 2019
Revised: March 19, 2020
Published: April 6, 2020

https://dx.doi.org/10.1021/acs.jpcb.9b12013
J. Phys. Chem. B 2020, 124, 3371−3386

which results from stronger thermodynamic affinity between different species in the mixture, making the liquid mixture more stable than the pure species. Likewise, a positive or minimum boiling azeotrope indicates less favorable interactions and a less stable liquid mixture. Azeotropes of binary mixtures have been extensively studied over the decades with well established experimental data sets[10−12] and thermodynamic models in the literature (such as Wilson, NRTL, UNIQUAC, UNIFAC, et al.[3,13−15]). Compared with getting the phase-diagram data, establishing the molecular mechanism is more difficult.

Since an azeotrope can be interpreted as either the most (negative azeotrope) or the least (positive azeotrope) stable liquid mixture, there has been a natural focus on the liquid structure of the exact azeotrope point. In particular, it is intuitive to speculate the existence of special molecular arrangements (commonly described as "clusters") that dominate the liquid azeotropic mixture. Such clusters are, presumably, formed between different species with stoichiometric ratio and will be hereinafter referred to as "co-clusters", which is to be differentiated from clusters of molecules of the same species discussed later in the paper. This concept is especially convenient for negative azeotropes where clustering between unlike molecules is expected to lead to liquid structures that are thermodynamically more stable. Experimentally, this concept has been probed with techniques such as infrared spectroscopy (IR),[16,17] mass spectroscopy (MS),[18] Raman spectroscopy,[19] nuclear magnetic resonance spectroscopy (NMR),[20,21] X-ray diffraction,[22] inelastic neutron spectroscopy,[19] and Fourier-transform infrared spectroscopy (FT-IR).[23,24] In this view, the liquid structure at the azeotrope is conceived to be composed of unit coclusters, each of which has a well-defined stoichiometric ratio between the two types of molecules in the mixture. For example, Jalilian used FT-IR and ^{1}H NMR to study the acetone/chloroform azeotropic mixture and compared it with pure acetone and pure chloroform.[23] They found that the $\delta(^1\mathrm{H})$ shift occurs at a higher frequency in the azeotrope than it does in pure acetone or chloroform, which was considered a sign for the formation of acetone−chloroform molecular coclusters. The proposed unit structure contains two chloroform molecules connected with one acetone molecule by two type of hydrogen bonds (HBs): one between the hydrogen in chloroform and the oxygen in acetone and the other between one methyl hydrogen of acetone and one chlorine in chloroform. A number of other azeotropic systems, such as acetone/*n*-pentane,[25] methanol/benzene,[26] acetone/cyclopentane,[27] and acetone/cyclohexane,[28] were similarly studied. Without direct molecular images of such unit coclusters, their structures were commonly deduced from the number and type of available hydrogen-bond binding sites of both molecules. Theoretical arguments can also be made through, e.g., the density functional theory (DFT), which calculates the potential energy of prespecified unit cocluster configurations. Ripoll et al.[29] performed DFT calculation on coclusters of water/diethyl carbonate (DEC) at different stoichiometric ratios and found that the one with a 3:1 ratio is most stable, which agrees with the experimentally measured $x_{water} \approx 0.75$ at the azeotrope. Similar calculations were reported for methanol/benzene,[30] ethanol/isooctane,[31] hydrogen fluoride/water,[32] ethanol/water,[33] etc.

Despite its apparent appeal, especially in terms of explaining the azeotropic composition on the basis of the stoichiometric ratio in the unit coclusters, limitations of this idea are also evident. The concept of a unit cocluster at the azeotropic composition being energetically favorable resonates with that of a unit cell in a cocrystal structure, except that the mixture here is fundamentally still a liquid−local composition fluctuations would constantly disturb any ordered coclusters should they ever emerge. As such, the concept of coclusters is not well-defined and is hard to verify in real disordered liquid structures. Indeed, direct evidence for ordered cocluster structures with a clear stoichiometric ratio of the two components has not been found. Meanwhile, the proposed existence of such coclusters would only explain the relative thermodynamic stability of the azeotropic composition (and from an energetic argument only) and thus its lower vapor pressure compared with the ideal-mixture limit, which, by itself, is a necessary condition for a negative azeotrope but not a sufficient one. It would also struggle to explain a positive azeotrope where the unit coclusters would have to be less stable than a completely random mixture.

Recently, Shephard et al.[34] reported a detailed investigation of the liquid structure at the azeotropic composition for both a positive (methanol/benzene) and negative (acetone/chloroform) azeotrope system with neutron scattering and the diffraction data were converted to a detailed molecular representation with the empirical potential structure refinement (EPSR) modeling approach[35,36] (which fits the molecular model to diffraction data with a Monte Carlo (MC) algorithm). Clear differences were found in the structural patterns of these two types of azeotropes. For methanol/benzene, strong association is found between methanol molecules. Inserting benzene molecules at the azeotropic composition does not lead to the formation of binary coclusters proclaimed by the cocluster theory. Rather, clustering still occurs between methanol molecules and benzene molecules are largely left out of methanol-rich regions. Meanwhile, for acetone/chloroform, the two components interact through both HB (acetone-O and chloroform-H) and halogen-bond (acetone-O and chloroform-Cl) interactions, which leads to a moderate increase of cross-species association at the azeotrope compared with a random mixture and explains its relative stability. However, clear ordered coclusters are still absent.

We note that the defining difference between an azeotropic mixture and a general nonideal one is whether the relative volatilities of the two components switch places. In a nonazeotropic mixture (ideal or nonideal), the component with higher vapor pressure in its pure form is consistently more volatile in the mixture for the entire composition range, whereas in an azeotropic mixture, the component more volatile before the azeotrope becomes less volatile after the azeotrope. A molecular mechanism for an azeotrope will have to explain this transition, which requires us to go beyond the azeotropic point and examine the entire range of composition. Fewer experimental efforts have been reported on this front. Wakisaka[37−39] used mass spectroscopy to analyze and compare the patterns of molecular organization in an ethanol/water mixture before and after the azeotrope. They proposed that at lower $x_{ethanol}$, the liquid structure is dominated by strong water−water hydrogen-bonding interactions and thus ethanol is more volatile. At higher $x_{ethanol}$ the scenario is reversed and thus water becomes more volatile. This argument, of course, only applies to mixtures of two polar components each with strong self-interactions.

https://dx.doi.org/10.1021/acs.jpcb.9b12013
J. Phys. Chem. B 2020, 124, 3371−3386

Molecular simulation provides direct access into the microscopic molecular structures and detailed intermolecular interactions that are only inferred indirectly in experiments. It has been widely used in the study of liquid thermodynamics for the prediction of their phase behaviors and thermodynamic properties and for fundamental inquiries into the underlying molecular mechanisms.[40−42] For azeotrope research, however, previous efforts mostly focused on its prediction as well as the prediction of the VLE phase diagram. The potential of molecular simulation for its mechanistic understanding has not been fully exploited. Azeotropes were captured in molecular simulation as early as the study of the carbon dioxide/ethane system using a Lennard-Jones (L-J) model by Scalise et al.[43] Several simulation techniques have since been applied to azeotrope research. One example is the Gibbs−Duhem integration (GDI) method,[44] which was successfully applied by Pandit and Kofke[45] to capture azeotropes modeled by different L-J model parameters. Its accuracy for phase-equilibrium prediction depends strongly on the initial condition for integration[46,47] and it also fails to capture the critical-point phenomenon.[44,45,48] Another method is histogram-reweighting Monte Carlo (HrMC),[49] which accurately predicts the location of azeotropic points in ethane/perfluoroethane, propanal/*n*-pentane, and acetone/*n*-hexane mixtures.[50,51] However, for many other mixtures, such as acetone/chloroform, acetone/methanol, and chloroform/methanol, azeotrope prediction by HrMC was found to be rather inaccurate.[52] The most widely used method in this area is the Gibbs ensemble Monte Carlo (GEMC) method,[40] which has been applied to the VLE of a wide range of azeotropic mixtures, such as ethanol/water,[53] methanol/*n*-hexane,[54] ethanol/*n*-hexane,[54] 1-pentanol/*n*-hexane,[55] methanol/acetonitrile,[56] 1-propanol/acetonitrile,[55] ethyl acetate/ethanol,[57] and methanol/ethyl acetate.[57] The success of the GEMC approach established an efficient and reliable way for predicting azeotropes given sufficiently accurate force-field parameters for the molecules involved.

Overall, although an azeotrope is a well-known thermodynamic phenomenon of much practical significance, fundamental understanding into its molecular origin is rather limited. There has been a historical emphasis on explaining its existence through its strong departure from the ideal-mixture behavior, which has led to a focus on the liquid structure at the azeotropic composition. Many of those efforts were targeted at identifying the molecular arrangement, often conjectured to be coclusters formed by different species with a stoichiometric ratio, responsible for the raised or reduced volatility (vapor pressure) compared with the Raoult's law. We will instead focus on the qualitative feature that distinguishes azeotropic mixtures from nonazeotropic ones—the changing relative volatility between components. In this study, a thermodynamic criterion for the occurrence of an azeotrope is developed on the basis of this perspective and used as the guidance for its molecular understanding. GEMC simulation is performed on the ethanol/benzene system as a representative example of a positive azeotrope formed by a polar/nonpolar pair. The full VLE phase diagram is successfully reproduced in our simulation including the occurrence of an azeotrope, which to our knowledge has not be reported before for this system. Molecular interactions are analyzed according to the thermodynamic criterion. Changes in molecular energetics are then traced back to the changing liquid-phase structure for the entire composition range. It is revealed that at different compositions, the molecular arrangement undergoes transitions between distinct stages, which explains the changing thermodynamic properties and eventually the occurrence of an azeotrope. This is to our knowledge the first in-depth investigation, based on molecular simulation, into the molecular mechanism for azeotrope formation that connects the microscopic liquid structure to macroscopic thermodynamics. The molecular mechanism proposed here is expected to be generalizable for other positive azeotropes in binary mixtures between polar and nonpolar species.

2. SIMULATION DETAILS

The TraPPE-UA (Transferable Potentials for Phase Equilibria-United Atoms) force field[58,59] is applied to model ethanol and benzene molecules. This is a united-atom (UA) model in which the H atoms in CH_3, CH_2, and aromatic CH(aro) are grouped with their host C as bundled pseudoatoms, whereas the hydroxyl H is modeled as a separate point charge. The pairwise-additive L-J 12-6 potential combined with Coulombic interactions between partial charges is used to describe nonbonded interactions

$$u_{\text{nonbonded}}(r_{ij}) = 4\epsilon_{ij}\left[\left(\frac{\sigma_{ij}}{r_{ij}}\right)^{12} - \left(\frac{\sigma_{ij}}{r_{ij}}\right)^{6}\right] + \frac{q_i q_j}{4\pi\epsilon_0 r_{ij}} \tag{3}$$

where ϵ_0 is the vacuum permittivity, i and j are atom indices, q_i and q_j are the partial charges of atoms i and j, r_{ij}, ϵ_{ij}, and σ_{ij} are their separation distance, LJ energy well depth, and LJ length scale, respectively. The Lorentz−Berthelot combination rule[60,61] is used to determine the cross-interaction LJ parameters between unlike atoms

$$\sigma_{ij} = (\sigma_{ii} + \sigma_{jj})/2 \tag{4}$$

$$\epsilon_{ij} = \sqrt{\epsilon_{ii}\epsilon_{jj}} \tag{5}$$

A cutoff of 14 Å was applied to the nonbonded pairwise interactions with an analytical tail correction to minimize the truncation error in the LJ interaction.[62,63] The Ewald summation with a tinfoil boundary condition was used to calculate the long-range electrostatic potential[62] using the same settings as Wick et al.[64] and Chen et al.[54]

In the TraPPE-UA force field, all bond lengths are fixed, but a harmonic potential is used to describe the bending resistance of bond angles

$$u_{\text{bend}} = \frac{k_\theta}{2}(\theta - \theta_0)^2 \tag{6}$$

where θ, θ_0, and k_θ are the measured bond angle, the equilibrium bending angle, and the force constant, respectively. Meanwhile, a torsion potential is applied to control the dihedral rotation around bonds,

$$u_{\text{tors}} = c_0 + c_1[1 + \cos(\phi)] + c_2[1 - \cos(2\phi)] + c_3[1 + \cos(3\phi)] \tag{7}$$

where c_0, c_1, c_2, and c_3 are the dihedral interaction coefficients and ϕ is the dihedral angle. All nonbonded and bonded potential parameters are taken from refs 54 and 64 and are listed in Table 1 and Table 2.

Constant-temperature constant-pressure GEMC simulation, involving coupled−decoupled configurational-bias Monte Carlo (CBMC) sampling moves,[65,66] was employed to

https://dx.doi.org/10.1021/acs.jpcb.9b12013
J. Phys. Chem. B 2020, 124, 3371−3386

Table 1. Nonbonded Interaction Parameters for Ethanol and Benzene in the TraPPE-UA Force Field[54,64]

(pseudo-)atom	molecule	σ [Å]	ϵ/k_B [K][a]	q [e]
CH_3	ethanol	3.750	98	
CH_2	ethanol	3.950	46	+0.265
CH(aro)	benzene	3.695	50.5	
O	ethanol	3.020	93.0	−0.700
H (in OH)	ethanol			+0.435

[a] k_B is the Boltzmann constant.

Table 2. Bonded Interaction Parameters for Ethanol and Benzene in the TraPPE-UA Force Field[54,64]

bond length		r_0 [Å]	
CH_3–CH_2		1.540	
CH_2–O		1.430	
O–H		0.945	
CH(aro)–CH(aro)		1.400	
bond angle		θ_0 [deg]	k_θ/k_B [K]
CH_3–CH_2–O		109.47	50400
CH_2–O–H		108.50	55400
CH(aro)–CH(aro)–CH(aro)		120.00	rigid
torsion angle	c_0/k_B [K]	c_1/k_B [K]	c_2/k_B [K]	c_3/k_B [K]
CH_3–CH_2–O–H	0	209.82	−29.17	187.93

compute the VLE of ethanol/benzene mixtures at 15 composition levels (hereinafter, liquid-phase mole fractions are denoted by x_i, where i = 1 for ethanol and i = 2 for benzene). The simulation pressure was set to 1 atm for all compositions (which means the temperature of VLE varies). The total number of these two types of molecules was controlled at 450, and these molecules were initially allocated between the two simulation cells (one for the liquid phase and one for the vapor phase) at random. In either cell, molecules were placed on a cubic lattice in the initial configuration. For each simulation, 80 000 MC cycles were used to equilibrate the system, followed by another 30 000 cycles for the production run. Each cycle contains 450 MC moves. Both the initial configuration generation and the GEMC simulation were performed using the MCCCS Towhee program.[58,59] The converged liquid cell has a dimension of approximately 30 × 30 × 30 Å. The block averaging approach was used for uncertainty analysis:[67] the production run was divided into five equal blocks, and the standard error between the block averages is reported as the simulation uncertainty. Five types of MC moves were used in the sampling:[54,55,58,64,68−70] volume exchanges and CBMC molecular swaps between the two cells, CBMC conformational bias moves, and molecular translations, and rotations. Each MC move was randomly selected with a 0.1−1% probability for volume exchange and 20−30% for molecule swap moves; the remaining probability was evenly divided between conformation bias moves, translations, and rotations.

3. RESULTS AND DISCUSSION

3.1. Vapor−Liquid Phase Diagram. The temperature−composition VLE diagram from our simulation is plotted in Figure 1 and compared with the earlier experimental data of Gao et al.[71] The simulation results can well capture the shape of the experimental curves and reasonably predict the azeotrope composition ($x^{aze}_{1,sim} \approx 0.389$ vs $x^{aze}_{1,exp} \approx 0.450$). The predicted azeotropic temperature of T^{aze}_{sim} = 340.45 K is

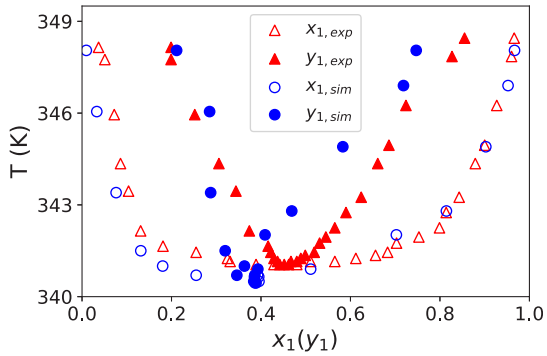

Figure 1. Comparison of the vapor−liquid equilibrium (VLE) phase diagram (1 atm) from our simulation (circles) with the experiments of Gao et al.[71] (triangles): 1, ethanol; 2, benzene. Error bars are smaller than the marker size and thus not shown..

strikingly close to the experimental value of T^{aze}_{exp} = 341.15 K. The TraPPE-UA force field was used by Wick et al.[64] and Chen et al.[54] to study the thermodynamic properties of pure ethanol and benzene, in which the predicted normal boiling point of ethanol was pretty accurate (353 K in simulation vs 351.4 K in experiments) while that of benzene was somewhat underestimated (341 K in simulation vs 353.1 K in experiments). As such, the force field is adequately accurate for these two compounds and a slight shift to lower temperatures is expected in the temperature−composition phase diagram of their mixtures. The moderate quantitative error between simulation and experiments in the predicted x^{aze}_1 is mostly attributable to errors in the vapor-phase composition. Although the ethanol/benzene azeotropic mixture has not been previously studied with molecular simulation, the level of prediction errors observed here is on par with other mixtures studied in the literature.[54−57] Meanwhile, compared with most previous studies of mixtures by TraPPE-UA,[52,54,55,64,68,69] where the vapor−liquid coexistence region from simulation is often larger than that measured in experiments, this artifact is not obvious in our results. Overall, we conclude that the VLE and azeotrope phenomenon of ethanol/benzene are well reproduced by GEMC simulation with the TraPPE-UA force field, based on which we will further investigate the molecular origin of the azeotrope.

3.2. Thermodynamic Criterion for Azeotrope Existence. As laid out in the Introduction, our approach toward understanding the azeotrope is to focus not on the deviation from the ideal-mixture behaviors (i.e., in the case of the positive azeotropic system of ethanol/benzene, its lower boiling point compared with the Raoult's law), but on the changing relative volatility between the two components before and after the azeotrope. In our current system (Figure 1), at $x_1 < x^{aze}_1$, ethanol remains the more volatile component (i.e., at given temperature, ethanol's mole fraction in the liquid phase x_1 is lower than that in its coexisting vapor phase y_1), but after the azeotrope, benzene takes over and has a higher tendency to vaporize ($x_1 > y_1$). Our goal is to reveal the molecular origin behind this switch of relative volatility, which only occurs at the azeotrope. Note that azeotropes can occur even when the vapor phase is an ideal gas. At ambient pressure studied here, it is a phenomenon solely driven by liquid-phase mixture thermodynamics. Therefore, we focus on the changes in the thermodynamic properties and molecular arrangement, before and after the azeotrope, in the liquid phase only.

https://dx.doi.org/10.1021/acs.jpcb.9b12013
J. Phys. Chem. B 2020, 124, 3371−3386

We start from the fundamental criterion for azeotropes and derive the corresponding relations in terms of the thermodynamic properties of azeotropic mixtures. When a binary azeotrope appears, the composition of the liquid phase is equal to that of the vapor phase (eq 1). Assuming ideal gas for the vapor phase, the equilibrium compositions are related through the modified Raoult's law

$$y_1 P = x_1 \gamma_1 P_1^{\text{sat}} \tag{8}$$

$$y_2 P = x_2 \gamma_2 P_2^{\text{sat}} \tag{9}$$

Combining these two equations, the relationship between the activity coefficients, γ_i, and the corresponding vapor pressure of the pure species, P_i^{sat}, is written to be

$$\frac{\gamma_1}{\gamma_2} = \left(\frac{y_1}{x_1}\right)\left(\frac{x_2}{y_2}\right)\frac{P_2^{\text{sat}}}{P_1^{\text{sat}}} \tag{10}$$

At the azeotrope, eq 1 is invoked. Taking the logarithm of both sides, we get

$$\ln \frac{P_2^{\text{sat}}}{P_1^{\text{sat}}} = \ln \frac{\gamma_1}{\gamma_2} = \ln \gamma_1 - \ln \gamma_2 = \frac{\bar{G}_1^{\text{E}}}{RT} - \frac{\bar{G}_2^{\text{E}}}{RT} \quad (\text{when } x_1 = x_1^{\text{aze}}) \tag{11}$$

where the last equality comes from the thermodynamic relation,

$$\bar{G}_i^{\text{E}} = RT \ln \gamma_i \tag{12}$$

$\bar{G}_i^{\text{E}}$ is the partial excess Gibbs free energy of component i (the overbar denotes partial molar properties and superscript "E" represents excess properties (i.e., departure from the ideal mixture)) and R is the ideal-gas constant. For a positive azeotrope, before the azeotropic point, $x_1 < y_1$ and $y_2 < x_2$, and after the azeotropic point, $x_1 > y_1$ and $y_2 > x_2$. Therefore, the relationship between P_i^{sat} and $\bar{G}_i^{\text{E}}$ is as follows:

$$\begin{cases} \dfrac{\bar{G}_1^{\text{E}}}{RT} - \dfrac{\bar{G}_2^{\text{E}}}{RT} > \ln \dfrac{P_2^{\text{sat}}}{P_1^{\text{sat}}} & (\text{when } x_1 < x_1^{\text{aze}}) \\ \dfrac{\bar{G}_1^{\text{E}}}{RT} - \dfrac{\bar{G}_2^{\text{E}}}{RT} < \ln \dfrac{P_2^{\text{sat}}}{P_1^{\text{sat}}} & (\text{when } x_1 > x_1^{\text{aze}}) \end{cases} \tag{13}$$

where P_i^{sat} can be easily estimated with the Antoine equation[72]

$$\ln P_i^{\text{sat}} = A_i - \frac{B_i}{C_i + T} \tag{14}$$

at the targeted temperatures (A_i, B_i, and C_i are species-specific parameters). $\bar{G}_i^{\text{E}}$ is calculated from its definition

$$\bar{G}_i^{\text{E}} \equiv \bar{G}_i - G_i^{\text{id}} \tag{15}$$

where $\bar{G}_i$ is the partial molar Gibbs free energy (i.e., chemical potential) directly collected from the GEMC simulations. Its counterpart in an ideal mixture can also be calculated:

$$G_i^{\text{id}} = G_i + RT \ln x_i \tag{16}$$

in which the pure-species molar Gibbs free energy G_i is computed by building and equilibrating a pure liquid cell of species i.[54,64]

The most important takeaway from eqs 11 and 13 is that azeotrope is marked by a crossover between the $(\bar{G}_1^{\text{E}} - \bar{G}_2^{\text{E}})/(RT)$ vs x_1 and $\ln(P_2^{\text{sat}}/P_1^{\text{sat}})$ vs x_1 lines. For the benzene/ethanol system studied, these two quantities are calculated and plotted in Figure 2 for the entire composition range. The vapor pressure ratio of the two species is not sensitive to temperature, at least within the range of the VLE phase diagram; $\ln(P_2^{\text{sat}}/P_1^{\text{sat}})$ is nearly a flat line. Meanwhile, the partial excess Gibbs free energy difference between ethanol and benzene, $(\bar{G}_1^{\text{E}} - \bar{G}_2^{\text{E}})/(RT)$, decreases monotonically: it starts above the $\ln(P_2^{\text{sat}}/P_1^{\text{sat}})$ line (i.e., component 1, ethanol, is more volatile) and steadily declines with increasing x_1 and intersects with the latter at around $x_1 = 0.4$, which matches the azeotrope point. This simply confirms the thermodynamic argument of eqs 11 and 13. In cases with negative azeotropes, the crossover would still take place but in an opposite direction: $(\bar{G}_1^{\text{E}} - \bar{G}_2^{\text{E}})/(RT)$ would rise from below $\ln(P_2^{\text{sat}}/P_1^{\text{sat}})$ and exceed the latter at the azeotrope. Meanwhile, for nonazeotropic systems, if $(\bar{G}_1^{\text{E}} - \bar{G}_2^{\text{E}})/(RT)$ is initially higher than $\ln(P_2^{\text{sat}}/P_1^{\text{sat}})$, it would stay so for the entire composition range, and vice versa.

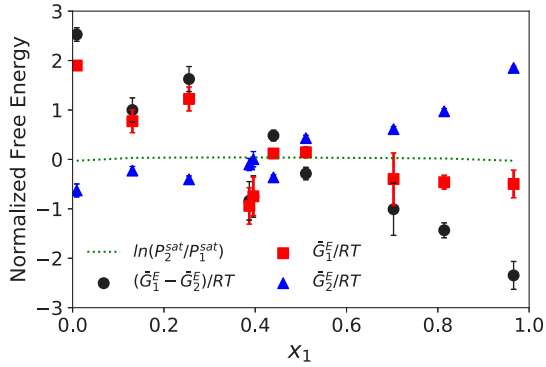

Figure 2. Partial excess Gibbs free energy analysis of the ethanol/benzene liquid mixture at VLE (see eqs 11 and 13 and related discussion): 1, ethanol; 2, benzene. Error bars smaller than the marker size are not shown.

The key of understanding azeotrope formation lies thus in the molecular origin for the drastic changes in the relative magnitudes of $\bar{G}_1^{\text{E}}$ and $\bar{G}_2^{\text{E}}$. Partial excess Gibbs free energies of the two components are thus also plotted separately in Figure 2. Interestingly, the seeming steady decline of $(\bar{G}_1^{\text{E}} - \bar{G}_2^{\text{E}})/(RT)$ is not solely attributed to either one of the components. Before the azeotrope, the decline is mostly dominated by the ethanol contribution $\bar{G}_1^{\text{E}}/(RT)$ while the benzene contribution $\bar{G}_2^{\text{E}}/(RT)$ remains roughly constant. After the azeotrope, the ethanol contribution starts to plateau while the continued decrease of $(\bar{G}_1^{\text{E}} - \bar{G}_2^{\text{E}})/(RT)$ is now driven by a rising second (benzene) term (especially at $x_1 \gtrsim 0.5$). This is somewhat surprising considering that ethanol is much more polar than benzene and has nontrivial HB interactions between its molecules. It would be more intuitive to expect ethanol molecules to display transitions in molecular arrangement patterns with its increasing mole fraction and thus more drastic variations in $\bar{G}_1^{\text{E}}/(RT)$ (than $\bar{G}_2^{\text{E}}/(RT)$).

3.3. Energetic Analysis. The most direct approach to interpret the free energy variations observed in Figure 2 is to dissect the partial excess Gibbs energy into enthalpic and entropic terms according to

$$\bar{G}_i^{\text{E}} \equiv \bar{H}_i^{\text{E}} - T\bar{S}_i^{\text{E}} = \bar{U}_i^{\text{E}} + P\bar{V}_i^{\text{E}} - T\bar{S}_i^{\text{E}} \tag{17}$$

https://dx.doi.org/10.1021/acs.jpcb.9b12013
J. Phys. Chem. B 2020, 124, 3371−3386

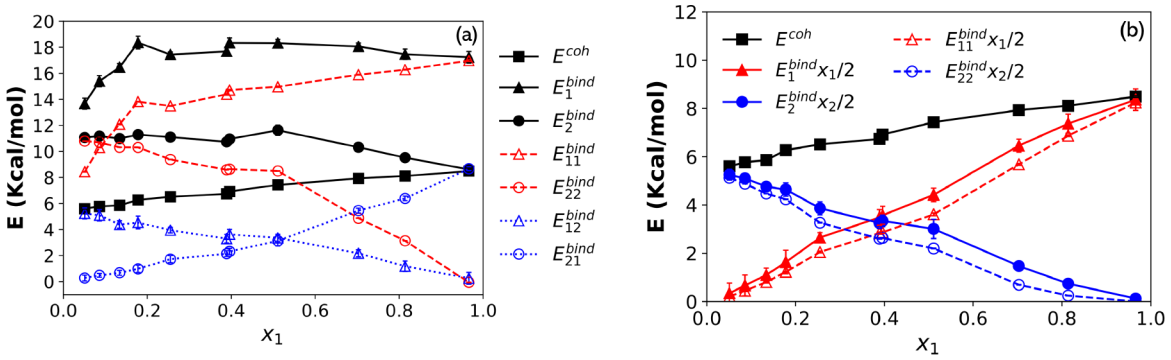

Figure 3. Breakdown of the cohesive energy of the ethanol−benzene liquid mixture at VLE and binding energies of the components: (a) contributions to the binding energy (see eqs 32 and 33) and (b) contributions to cohesive energy (see eq 34). Error bars smaller than the marker size are not all shown.

and analyze their individual contributions (where H, S, U, and V are symbols for enthalpy, entropy, internal energy, and volume, respectively, all on a per mole basis). Direct calculation of entropy from molecular simulation is a daunting task. Meanwhile, determination of partial enthalpy is also not straightforward; as discussed in Appendix A, partial property calculation in general is complicated for polyatomic molecular liquids.

Our analysis will instead focus on energetic quantities readily accessible from molecular simulation. We start with the concept of molar cohesive energy E^{coh}, which is defined as the energy required to pull apart all molecules in 1 mol of the liquid to infinite separation. As shown in Appendix A, this energy directly accounts for the total intermolecular interactions in the liquid, which must be broken to separate the molecules, i.e.

$$E^{coh} \approx -E^{inter} \tag{18}$$

The minus sign is because cohesive energy is defined on the basis of the liquid as the reference state; it is the energy change from the bulk liquid phase to a hypothesized state where molecules are isolated from one another (eq 25 in Appendix A). When intermolecular interactions are more attractive (lower E^{inter}), separating the molecules would cost more energy (higher E^{coh}). Contributions to the cohesive energy are attributable to each constituting component through a quantity we define as (for the lack of a better term) binding energy. The molar binding energy of component 1 E_1^{bind}, for example, describes the energy required to strip individual component-1 molecules from the liquid to infinite distance, scaled to the per mole (of component 1) basis, while keeping the remaining molecules unmoved. This hypothetical process only breaks the intermolecular interactions between the removed molecule and all other molecules in the liquid. Binding energy is related to cohesive energy via

$$E^{coh} = \frac{1}{2}(x_1 E_1^{bind} + x_2 E_2^{bind}) \tag{19}$$

as shown also in Appendix A (eq 34).

We postulate that component free energy variations in Figure 2 are dominated by binding energy changes, which means $-E_i^{bind}$ would capture major trends in the $\overline{G}_i^E$ profiles, even although their magnitudes may not be directly comparable. (The minus sign, again, is because binding energy is defined with the liquid state as the reference state.) According to eq 17, three assumptions are implied in our approach.

1. Contribution by entropy change is secondary, which is not to say that $-T\overline{S}_i^E$ must be small, but assume that its variation between different mixture composition is smaller than that of the enthalpy term.
2. Within enthalpy, contribution of the $P\overline{V}_i^E$ term is much smaller than that of energy.
3. Energy change associated with mixing, which is quantified by $\overline{U}_i^E$, is dominated by the changing intermolecular interactions, which means its major trends will be captured by $-E_i^{bind}$.

The first assumption is proposed considering the strong polar−polar interactions between ethanol molecules. Mixing ethanol with benzene disrupts those interactions, and this change is expected to be large. Although entropy change of mixing is substantial, eq 17 only concerns excess entropy, which measures the deviation from the ideal-mixing case. Therefore, variation of the $T\overline{S}_i^E$ term is small as long as the entropy change deviates from the ideal-mixing limit to a similar extent at different composition. The second assumption is a safe one for liquids near ambient conditions, where the PV term is generally much smaller than U in enthalpy. The last assumption is also plausible. For simple molecules like ethanol or benzene, mixing does not cause substantial molecular conformational change−thus, change in intramolecular energy is expected to be small. The whole idea can also be intuitively rationalized: when a molecule of component i feels stronger pulling from other molecules in the mixture, E_i^{bind} is higher, $\overline{E}_i$ is lower (lower energy corresponds to more favorable interactions), $\overline{G}_i$ is lower, and component i is less volatile.

Validity of these assumptions can only be tested by comparing the $\overline{G}_i^E$ profiles in Figure 2 with those of binding energy. The composition dependence of cohesive and binding energies of the liquid mixture at VLE is calculated and plotted in Figure 3a. Overall, E^{coh} slowly but steadily increases with x_1, which is expected because as the mixture becomes more polar with a higher portion of ethanol, the molecules are harder to be broken apart. By contrast, the binding energies of individual components do not share the same monotonic trend. For ethanol, E_1^{bind} initially increases but saturates to a plateau at medium to high x_1 regions. This is consistent with the $\overline{G}_1^E$ profile in Figure 2, which initially declines but later converges to a nearly flat line. The turning point observed here (E_1^{bind}) occurs at a somewhat lower x_1 value than that of $\overline{G}_1^E$, which may be attributed to the differences between these two

https://dx.doi.org/10.1021/acs.jpcb.9b12013
J. Phys. Chem. B 2020, 124, 3371−3386

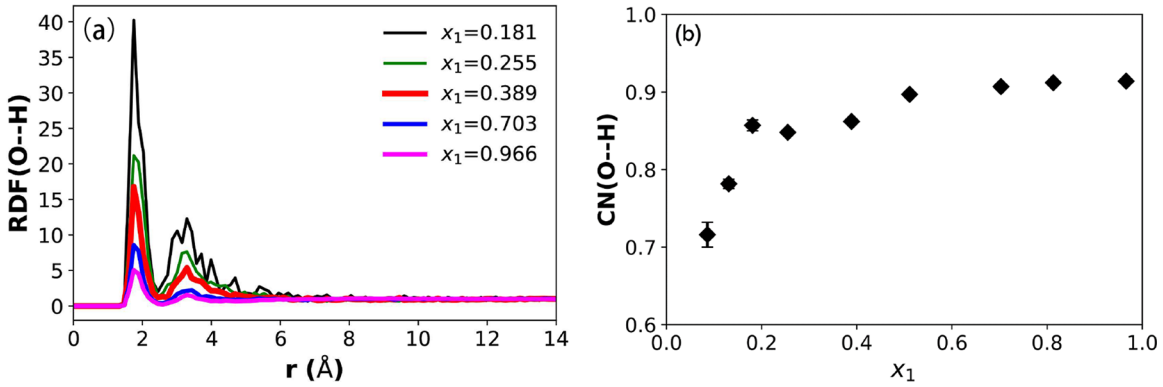

Figure 4. Arrangement of hydroxyl H atoms around hydroxyl O atoms between ethanol molecules (i.e., atom pairs belonging to the same OH group are excluded) in the liquid phase at VLE: (a) radial distribution function (RDF; lower profiles correspond to higher x_1); (b) coordination number (CN; r_{valley} = 2.45 Å). In (b), error bars smaller than the marker size are not shown.

quantities such as the entropy component in $\overline{G}_i^E$. Similarly for benzene, E_2^{bind} is initially in a plateau but starts to decrease at $x_1 \approx 0.5$ (shortly after the azeotrope point at $x_1^{aze} = 0.389$), which closely reflects the trend of $\overline{G}_2^E$ in Figure 2.

It is clear that binding energy profiles of the components capture the most important trends in partial excess Gibbs energy, suggesting that the formation of the azeotrope, driven by the variation of $(\overline{G}_1^E - \overline{G}_2^E)/(RT)$, can be explained from an energetic argument. In particular, Figure 2 showed that, somewhat unexpectedly, the change of relative volatility between the two components over different compositions has two separate driving mechanisms: (1) the initial decrease of ethanol volatility (decrease of $\overline{G}_1^E$ at small x_1) corresponds to the increases in its binding energy E_1^{bind} and (2), after the $\overline{G}_1^E$ and E_1^{bind} plateau, the continued shift of volatility is overtaken by the increasing volatility of benzene $\overline{G}_2^E$ and its lowering binding energy E_2^{bind}.

Binding energy is further broken down to contributions from self- and cross-interactions

$$E_1^{bind} = E_{11}^{bind} + E_{12}^{bind} \tag{20}$$

$$E_2^{bind} = E_{22}^{bind} + E_{21}^{bind} \tag{21}$$

(detailed mathematical definitions are given in eqs 32 and 33 in Appendix A), which is also shown in Figure 3a. The initial high-slope increase of E_1^{bind} is mainly driven by the interaction with other type 1 (ethanol) molecules, i.e., the E_{11}^{bind} term, which is expected because of the strong polar−polar (such as HB) interactions. The increase in E_{11}^{bind}, however, slows down after $x_1 \approx 0.2$, marking the end of the first driving mechanism discussed above. Meanwhile, the ethanol−benzene interaction contribution E_{12}^{bind} decreases monotonically, roughly proportional to the decreasing mole fraction of benzene. Its slope is small compared with the initial rapid rise in E_{11}^{bind} but is sufficient to offset the slower ramp in the latter after $x_1 \approx 0.2$, resulting in the plateau in the overall E_1^{bind}. For benzene, the initial plateau of E_2^{bind} also results from the compensation of the decreasing self-interaction E_{22}^{bind} by the increasing cross-interaction with ethanol E_{21}^{bind}. Indeed, the E_{22}^{bind} profile is nearly parallel to the E_{12}^{bind} one in that regime as both drop as a result of having fewer benzene molecules around. At $x_1 \gtrsim 0.5$, the drop of E_{22}^{bind} takes a sharper slope, indicating that the arrangement of benzene molecules has fundamentally changed and the lowering self-interaction can no longer be solely accounted for by the decreasing percentage of benzene in the mixture. This leads to the overall decline of E_2^{bind} and, eventually, of $\overline{G}_2^E$.

Finally, Figure 3b shows the breakdown of the cohesive energy into binding energy of components according to eq 19: E^{coh} is clearly the sum of $x_1E_1^{bind}/2$ and $x_2E_2^{bind}/2$ over the entire composition range. The dashed lines show the component contributions to the cohesive energy if the self-interaction terms, $x_1E_{11}^{bind}/2$ and $x_2E_{22}^{bind}/2$, are considered alone (i.e., neglecting cross-interaction contributions). Comparison with the solid lines shows that cross-interactions between different species contribute a very low proportion to the total cohesive energy. We may also see from Figure 3a that E_{12}^{bind} is significantly lower than E_{11}^{bind} for the entire composition range, whereas E_{21}^{bind} is lower than E_{22}^{bind} until $x_1 \gtrsim 0.7$. Dominance of self-interaction in both components suggests that ethanol (1) and benzene (2) molecules are not uniformly distributed across the space. Ethanol molecules are much more likely to closely interact with other ethanol molecules for all x_1 levels while benzene molecules also tend to group with their own kind until their mole fraction x_2 is very low.

3.4. Micro-Structure Analysis. We now analyze the microscopic origin, in terms of molecular arrangement patterns, for the energetic variations responsible for the azeotrope. Although the gathering of ethanol molecules is very much expected due to their strong polarity and mutual interaction, strong binding between them would only predict a continuous decrease of ethanol volatility. We have already shown that the azeotrope occurs as a combined outcome of the lowering ethanol volatility at low x_1 and raised benzene volatility at high x_1. The plateauing of E_1^{bind} and the decay of E_2^{bind} at medium to high x_1 regimes are not explained by this naive picture considering ethanol−ethanol interaction alone.

3.4.1. Molecular Organization. We start with the radial distribution function (RDF) $g(r)$ between the oxygen atom in ethanol and the hydroxyl hydrogen of a different ethanol molecule in Figure 4a. It measures the average number density of hydroxyl H at distance r from a hydroxyl O with which it does not share a bond, normalized by the domain-average number density of hydroxyl H. In all profiles, a clear peak is found at $r \approx 1.8$ Å, the typical length of a HB.[73,74] It is followed by a secondary peak at around $r \approx 3.4$ Å, likely from another ethanol molecule connected to the pair through consecutive HB interactions. Formation of small clusters of ethanol molecules in the nonpolar solvent of benzene is very much expected. What is surprising, however, is that the peak

https://dx.doi.org/10.1021/acs.jpcb.9b12013
J. Phys. Chem. B 2020, 124, 3371−3386

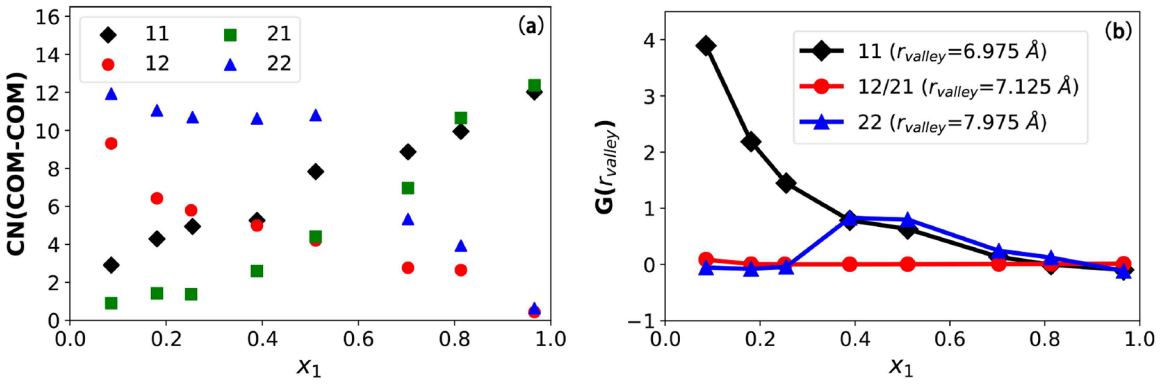

Figure 5. Molecular arrangement in ethanol/benzene liquid mixtures at VLE (measured by the center of mass positions of the molecules): (a) coordination number (CN); (b) Kirkwood−Buff integral (KBI) at $r = r_{valley}$. Measurements are made within the first solvation shell ($r < r_{valley}$) between molecules of the same and opposite species. Species 1 and 2 label ethanol and benzene, respectively, and CN_{12}, e.g., measures the distribution of benzene around ethanol molecules. Error bars are smaller than the marker size and thus not shown.

amplitude decreases with increasing ethanol mole fraction x_1. Indeed, except the lowest mole fraction level $x_1 = 0.008$ simulated in this study, where HBs are not significant, a strong primary peak is found at all other x_1 levels. For the second lowest $x_1 = 0.086$, the peak is much higher than those shown in Figure 4a and thus not included in the plot. This indicates that ethanol molecules start to assemble with one another through HB interactions at very low mole fractions. As more ethanol molecules are introduced to the mixture, the chance of HB formation does not rise proportionally.

The average number of particles of type j in a spherical shell around a central atom of type i (i.e., the coordination number (CN)) is calculated from $g_{ij}(r)$ with

$$\mathrm{CN}_{ij} \equiv 4\pi\nu_j \int_0^{r_{\mathrm{valley}}} g_{ij}(r) r^2 \, \mathrm{d}r \tag{22}$$

where ν_j is the domain-average number density of type j; r_{valley} is the minimum position between the first and second peaks in the $g_{ij}(r)$ profile which defines the outer boundary of the first solvation shell. The CN of hydroxyl H (j) around nonbonding hydroxyl O (i) is plotted in Figure 4b. The number increases rapidly at the beginning, but after $x_1 \approx 0.2$, the rise slows down drastically. For $x_1 \gtrsim 0.5$, it essentially flattens. Since the first solvation shell in this case covers the length of a typical HB, this observation again indicates that HBs are formed at very low x_1, which quickly saturates with increasing x_1. Dependence of HB statistics on mixture composition will be more directly investigated below in section. 3.4.2.

We turn now to the spatial arrangement between whole molecules. RDFs can be calculated using the center of mass (COM) positions of both types of molecules from which CNs are calculated to examine the distribution patterns between different molecular pairs. As shown in Figure 5a, the benzene−benzene CN (22) is nearly flat at lower x_1 and only starts to descend at $x_1 \approx 0.5$. In a perfectly random (ideal-gas limit) mixture, molecules of both types would be uniformly distributed in the domain and this CN would decrease linearly with x_1 because of the lowering number density of benzene ν_2. Deviation from this behavior can only be attributed to nonuniform microscopic distribution of benzene molecules, which is most easily seen from the Kirkwood−Buff integral (KBI)[75]

$$G_{ij}(r) \equiv 4\pi \int_0^r (g_{ij}(r') - 1) r'^2 \, \mathrm{d}r' \tag{23}$$

shown in Figure 5b. Comparing eq 23 with eq 22 and noting that $g_{ij}(r) = 1$ when type j particles are completely uniformly distributed (i.e., no ij-interaction can affect its distribution, which is the ideal-gas limit), the KBI at $r = r_{valley}$ (as plotted in Figure 5b) can be interpreted as

$$G_{ij}(r_{\mathrm{valley}}) = \frac{\mathrm{CN}_{ij} - \mathrm{CN}_{ij}^{\mathrm{uniform}}}{\nu_j} \tag{24}$$

i.e., the difference between the actual CN and that of uniform distribution scaled by the particle number density. A positive $G_{ij}(r_{valley})$ indicates the accumulation of type j particles around type i ones within the first solvation shell while negative $G_{ij}(r_{valley})$ indicates the opposite. For benzene−benzene distribution, $G_{22}(r_{valley})$ is close to zero at the small x_1 (i.e., high x_2) limit, which is expected by considering that the distribution would be nearly uniform in a pure liquid. Aggregation between benzene molecules becomes clear at $x_1 \approx 0.255$, reaches a maximum at $x_1 \approx 0.4$, and starts to decrease at $x_1 \approx 0.5$. At the high x_1 or low x_2 limit ($x_1 \gtrsim 0.7$), the distribution is uniform again. Transition from the microscopic aggregation of benzene at $x_1 = 0.4$−0.5 to their uniform dispersion at higher x_1 causes the overall decrease in benzene−benzene interactions. Indeed, the CN_{22} profile in Figure 5a is rather similar to that of E_{22}^{bind} profile in Figure 3a and both have a downward turn at $x_1 \approx 0.51$. Analysis of benzene−benzene self-distribution patterns reveals the second driving mechanism for the changing relative volatility: at high x_1, ethanol molecules break the local benzene aggregates, which exposes individual benzene molecules to the less favorable benzene-ethanol interactions and thus increases their volatility.

For ethanol−ethanol distribution, $G_{11}(r_{valley})$ starts high at the low x_1 end and declines steadily with increasing x_1. At $x_1 \gtrsim 0.7$, ethanol distribution also becomes uniform as it approaches the pure liquid limit. The trend is consist with the earlier observation from O−H RDFs in Figure 4a that ethanol molecules start to cluster at extremely low x_1 but the degree of aggregation, somewhat unexpectedly, decreases with x_1 as the chance for HB binding saturates. This seeming perplexity, which will be further discussed below in section 3.4.2, becomes comprehensible considering that the distribution would have to return to near uniformity, i.e., $G_{11}(r_{valley}) \to 0$, at the $x_1 \to 1$

https://dx.doi.org/10.1021/acs.jpcb.9b12013
J. Phys. Chem. B 2020, 124, 3371−3386

limit. Unlike the benzene−benzene case, the CN_{11} profile differs considerably from the E_{11}^{bind} one: the latter shows a clear turning point at $x_1 \approx 0.2$ whereas the former is rather steady in its rise. Therefore, the transition point in E_{11}^{bind} and thus the changing volatility of ethanol (the first driving mechanism) cannot be solely accounted for by the changing spatial positions of neighboring ethanol molecules. The reason is that, compared with the benzene case, interactions between ethanol molecules are not dominated by the van der Waals (vdW) interaction which is more isotropic and determined by intermolecular distance. Rather, electrostatic interactions between the polar OH groups require specific relative orientations between ethanol molecules to form HBs. The importance of HB interactions in explaining the E_{11}^{bind} trend is affirmed by the CN_{OH} profile in Figure 4b where a clear turning point is identified at $x_1 \approx 0.2$, coinciding with that in the E_{11}^{bind} profile. Direct analysis of HB patterns will be performed in section 3.4.2.

Finally, for cross-species intermolecular arrangement, $G_{12}(r_{valley})$ (which equals $G_{21}(r_{valley})$) stays closer to zero for the entire composition range, indicating a weaker effect of cross-species interactions on molecular arrangement. Both CN_{12} and CN_{21} vary nearly linearly with composition, roughly in proportion to the corresponding number densities, ν_2 and ν_1. Both profiles show a small dip, a range of negative deviation, at $0.2 \lesssim x_1 \lesssim 0.5$, as a result of microscopic aggregation within the same species.

3.4.2. Hydrogen-Bonding Analysis. Observations made so far point toward a three-stage process behind the apparent steady decline of $(\bar{G}_1^E - \bar{G}_2^E)/RT$ (Figure 2). The first transition, between stages 1 and 2, occurs at $x_1 \approx 0.2$ and is marked by the plateauing of E_1^{bind}. The second transition, between stages 2 and 3, occurs at $x_1 \approx 0.5$, i.e., shortly after the azeotrope, and is responsible for the later drop of E_2^{bind}. The previous section (section 3.4.1) showed that the second transition can be explained by the dismantlement of benzene−benzene microscopic aggregation, which exposes benzene molecules to less favorable cross-species interactions with ethanol. However, the first transition is less clear from the spatial arrangement of ethanol molecules, as far as their RDF and KBI show. We note that ethanol−ethanol interaction is dominated by HB interactions, which are not determined by the COM positions of ethanol molecules alone. This section thus focuses on the direct analysis of HB formation patterns between ethanol molecules.

With the electron donor O and acceptor H atoms in the hydroxyl group, ethanol molecules can easily form HBs through which the possibility of forming molecular clusters or even networks is foreseeable. In this study, HBs are defined according to the classical geometric criterion[76−78] − a HB pair is identified when all of the following three conditions are met:

1. The distance between the O atoms on the two interacting −OH groups is ≤3.5 Å.
2. The distance between the donor O and acceptor H atoms is ≤2.6 Å.
3. The H−O···O angle is ≤30°.

Following this standard, the total number of HBs in the liquid cell N_{HB} can be found and the average number of HB connections seen by each ethanol molecule is $2N_{HB}/N_1$ (the factor of 2 is because each HB connects two ethanol molecules). As shown in Figure 6, ethanol starts to form HBs at very low concentration. (At the lowest ethanol concentration simulated, i.e., $x_1 = 0.008$, there are on average less than three ethanol molecules in the simulation cell and HBs are rare. That case is not shown in Figure 6 owing to the lack of statistics. The leftmost point in Figure 6 is $x_1 = 0.086$ where $2N_{HB}/N_1$ already exceeds 1.) Although the number of HBs connected to each molecule does initially increase with concentration, the increase rate tapers off very quickly: at $x_1 = 0.181$, $2N_{HB}/N_1$ reaches 1.359, which is not much lower than that of the highest concentration in Figure 6: $2N_{HB}/N_1 = 1.653$ at $x_1 = 0.966$. For comparison, Saiz et al.[79] calculated the HB statistics of pure ethanol from molecular dynamics results and at a very close temperature of $T = 348$ K, their $2N_{HB}/N_1 = 1.72$. Using a slightly different set of HB identification criteria and for a lower $T = 300$ K, Noskov et al.[80] reported the number to be 1.65 again for pure ethanol. Therefore, on average, each ethanol molecule has fewer than two HB connections and, from our results, it becomes clear that ethanol gets close to this final limit very early on, starting from $x_1 \approx 0.2$.

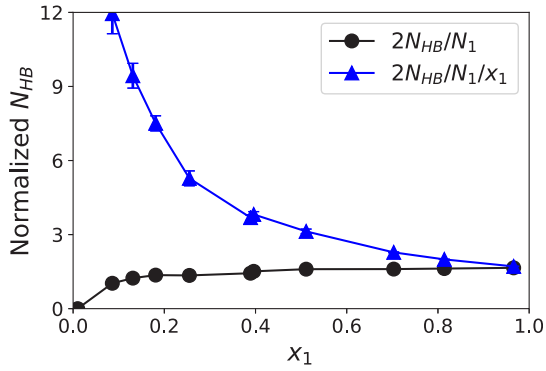

Figure 6. Composition dependence (in the liquid phase at VLE) of the average number of HB connections per ethanol molecule $2N_{HB}/N_1$ and the same number scaled by ethanol mole fraction $2N_{HB}/(x_1N_1)$. Error bars smaller than the marker size are not shown.

Since HB is a binary interaction, if we neglect the saturation of HB and resort to a simplistic mean-field argument, the chance for any one molecule to form HBs would be proportional to the concentration of other ethanol molecules in its surroundings, i.e., proportional to x_1. A scaled measure of the extent of HB formation is thus $2N_{HB}/(x_1N_1)$, which is also plotted in Figure 6. This number drops monotonically with increasing x_1 because of the early saturation of $2N_{HB}/N_1$: for an average ethanol molecule, once its number of HB connections gets close to (but lower than) two, connecting with additional ethanol molecules in its surroundings becomes drastically more difficult, even though there are many more of them around as x_1 increases. The decline of $G_{11}(r_{valley})$ with increasing x_1, as observed in Figure 5b, can be similarly explained. In eq 24, $CN_{11}^{uniform}$ strictly conforms to the mean-field argument and increases in proportion to x_1. For actual CN_{11}, surrounding ethanol molecules found around a reference ethanol molecule can be divided into two groups: (1) those forming HBs with the reference molecule and (2) additional molecules not HB-connected with the reference but happening to appear nearby. The number in group (2) is approximately proportional to x_1 (and thus to $CN_{11}^{uniform}$), whereas that of group (1) saturates to a nearly constant level at very low x_1. The KBI, as the difference between CN_{11} and $CN_{11}^{uniform}$ scaled by ν_1 (which is proportional to x_1), must thus decrease with x_1.

https://dx.doi.org/10.1021/acs.jpcb.9b12013
J. Phys. Chem. B 2020, 124, 3371−3386

Clusters formed by ethanol molecules interconnected through HBs can be identified by assigning any two molecules sharing at least one HB to the same cluster. The number-average ($\bar{N}_n$) and weight-average ($\bar{N}_w$) cluster sizes are plotted against x_1 in Figure 7. Both measures of cluster size initially

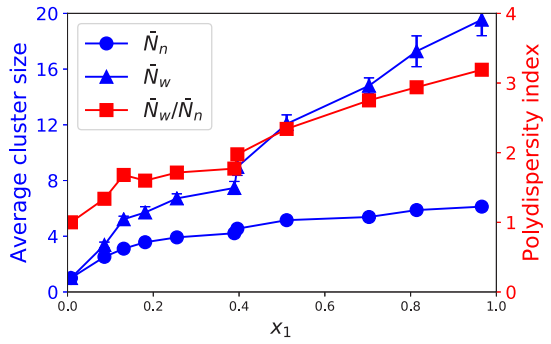

Figure 7. Composition dependence (in the liquid phase at VLE) of (left/blue) the number-average ($\bar{N}_n$) and weight-average ($\bar{N}_w$) size of ethanol HB clusters and (right/red) their polydispersity index (PDI) $\bar{N}_w/\bar{N}_n$. Error bars smaller than the marker size are not shown.

increase with ethanol concentration but after $x_1 \approx 0.2$ the trend significantly slows down. This transition is clearly associated with the near saturation of HB connections of each molecule, which also coincides with the slowdown of the rising ethanol–ethanol interaction contribution to binding energy E_{11}^{bind} at the same x_1 level (Figure 3a). Direct correspondence between HB statistics and E_{11}^{bind} is predictable as HB interactions are expected to dominate the ethanol–ethanol interactions. What is interesting is a clear separation of trends between $\bar{N}_n$ and $\bar{N}_w$ occurring around $x_1 \approx 0.4$ to 0.5, where $\bar{N}_w$ embarks on a new stage of steady growth while $\bar{N}_n$ stays nearly flat. The polydispersity index (PDI), defined as the ratio between the two, has plateaued before the transition but steadily rises afterward. This reflects a sudden increase of the portion of large-sized clusters in the distribution, which coincides with the second transition, between stages 2 and 3, marked by the isolation of benzene molecules (per discussion in section 3.4.1).

The probability density function (PDF) of cluster size is shown in Figure 8. For the whole range of x_1, the most probable size is 1; loose ethanol molecules are always present. If we only consider actual clusters (i.e., containing multiple

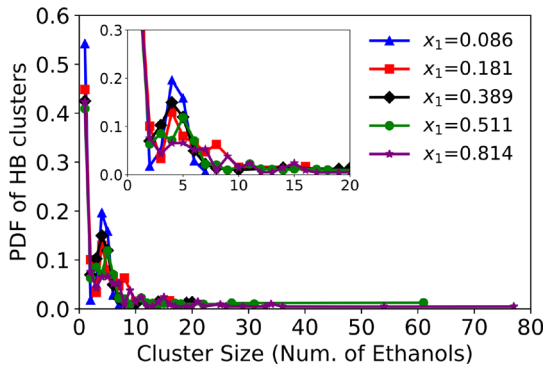

Figure 8. Probability density function (PDF) of HB cluster size in ethanol/benzene liquid mixtures at VLE. All data points represent nonzero values. An enlarged view is shown in the inset.

molecules), the most probable cluster size changes little and stays at 4–5 until very high x_1, with the $x_1 = 0.814$ case being the only exception in Figure 8. The increase of the average cluster size (Figure 7) is mostly contributed by a growing right tail. The distribution is very similar between $x_1 = 0.181$ and $x_1 = 0.389$, i.e., within stage 2 of the transitions ($0.2 \lesssim x_1 \lesssim 0.5$), while at $x_1 > 0.5$, an extended tail protrudes from the right end. The size of the largest cluster grows from 20 at $x_1 = 0.389$ to 61 and 77 at $x_1 = 0.511$ and $x_1 = 0.814$, respectively. (It is ultimately limited by the simulation domain size as we do not consider percolation (multiple periodic images of the same molecule in the cluster) in our cluster size measurement.) These "super" clusters likely result from the merger of smaller ones. Between $x_1 \approx 0.2$ and $x_1 \approx 0.5$, most clusters are formed by a few ethanol molecules and increasing x_1 must lead to a higher number density of such primary clusters. Shortening the distance between clusters facilitates their coalition. For a molecule to bridge two primary clusters, it only needs to have two HB connections, one with each primary cluster, which compared with the domain-average $2N_{\text{HB}}/N_1$ value is only slightly higher. Formation of a small number of super clusters through coalition can thus quickly bring up the weight-average cluster size $\bar{N}_w$ (Figure 7) without substantially affecting the average HB number (Figure 6), which is totally consistent with our observations.

Our finding here, that HB clusters continue to grow with x_1 beyond the azeotropic composition, contradicts the claim by Shephard et al.[34] that in the methanol–benzene system they studied using the EPSR modeling approach, methanol molecules form larger clusters at the azeotrope than in its pure state. In their results, methanol clusters with up to 20 molecules were found at the azeotrope, which is comparable to our $x_1 = 0.389$ case, but in pure methanol, the cluster size rarely exceeds 10. Other studies, however, have routinely reported large clusters containing $O(100)$ or more molecules in pure ethanol (and other small aliphatic alcohols as well), which varies with the system size, modeling method, and identification criteria.[81,82] In our highest $x_1 = 0.966$ case, the largest cluster contains 81 ethanol molecules, which is comparable to most previous studies despite our smaller system size and higher temperature.

Figure 9 shows the connectivity statistics of ethanol molecules measured by the number of HB connections each of them has. It is clear that HB structures are mostly developed

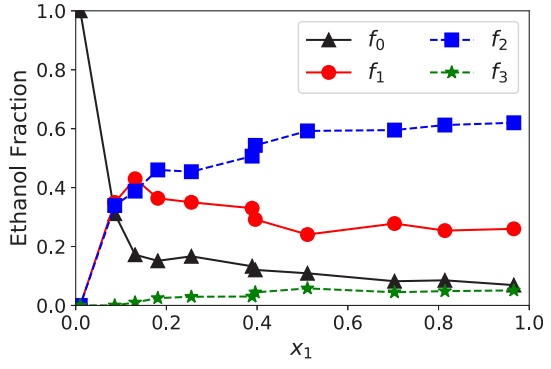

Figure 9. HB connectivity statistics of ethanol molecules in liquid mixtures with benzene at VLE. f_n is the fraction of ethanol molecules having n HB connections. The first point is at $x_1 = 0.008$; error bars are smaller than the marker size and thus not shown.

https://dx.doi.org/10.1021/acs.jpcb.9b12013
J. Phys. Chem. B 2020, 124, 3371–3386

at $x_1 < 0.2$ and, at larger x_1, changes of all statistics slow down. One exception is between $x_1 \approx 0.4$ and ≈0.5, where a notable drop in f_1 and increments in f_2 and f_3 are observed. Note that molecules having exactly one HB connection must be on the periphery or branch ends of clusters. Their reduction and the corresponding increase of molecules having two or more connections (i.e., those forming cluster cores) again reaffirms the coalition of small clusters at this composition range. At the highest $x_1 = 0.966$, 62% of the ethanol molecules have two HB connections, which is followed by 26% having one HB connection. This indicates that most HB clusters are chain-like structures where the middle members all have two connections and the end ones have one. Indeed, at least for pure methanol and ethanol, it has been well established in the literature that molecular chains are the predominant cluster form.[34,76,77,79] Only a very small portion (5.1%) of ethanol molecules have three connections that can serve as branching points in a cluster. The remaining 6.9% are loose molecules not attached to any cluster. This distribution is very much consistent with earlier analysis[79] of pure ethanol at $T = 348$ K where $(f_0, f_1, f_2, f_3) = (0.042, 0.245, 0.664, 0.049)$.

3.5. Molecular Picture. We have now collected all pieces in the jigsaw and are ready to put them together. A schematic of the overall molecular picture is presented in Figure 10. With

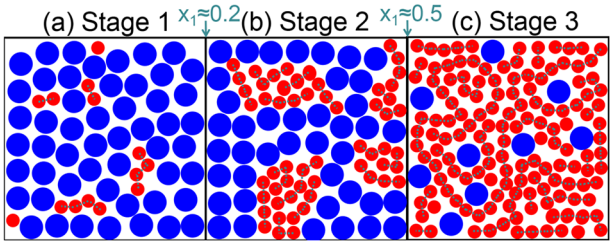

Figure 10. Schematics of liquid mircostructure evolution with increasing ethanol mole fraction at VEL: (red/small) ethanol; (blue/large) benzene. Stage 1: initial formation of HB clusters. Stage 2: microscopic segregation. Stage 3: isolation of benzene.

increasing ethanol fraction, the liquid mixture undergoes a three-stage transition of microstructure, which underlies the molecular energetics (Figure 3) and, ultimately, free energy (Figure 2) changes responsible for the occurrence of an azeotrope. At the limit of extreme dilution, ethanol molecules are isolated from one another: according to Figure 9, at $x_1 = 0.008$ (the lowest x_1 simulated here), $f_0 = 1$; i.e., all ethanol molecules are unassociated. However, they start to associate through HBs at very low concentrations. At x_1 as low as 0.086 (i.e., 8.6% of ethanol, the second most dilute case simulated), only about 31.1% of the ethanol molecules are still loose. The rest bind in small groups to form clusters "floating" in an "ocean" of benzene molecules (stage 1; see Figure 10a). Of course, such aggregates are dynamical in nature, but as long as the lifetime of HBs are longer than the diffusion time for a breakaway molecule to find another partner to bind with, clustering will be the norm. Within stage 1, the number of HBs per molecule quickly rises as HB clusters increase in both their number and size with increasing x_1. Because ethanol−ethanol interactions are dominated by HBs, its binding energy contribution E_{11}^{bind} also increases substantially in this regime, which makes ethanol less volatile.

Transition to stage 2 occurs at $x_1 \approx 0.2$, where most ethanol molecules are associated by HBs and further changes in all HB statistics slow down significantly. As ethanol concentration further increases, the number density of clusters is higher. Ethanol clusters and loose molecules tend to accumulate, leading to microscopic segregation between ethanol- and benzene-rich regions, which is reflected in the KBI magnitudes (Figure 5b).

After $x_1 \approx 0.5$ (i.e., stage 3), closely packed primary clusters start to coalesce, which, as discussed above, does not significantly raise the average number of HB connections per molecule and thus E_{11}^{bind} changes little in this regime. It is more clearly reflected in the cluster size distribution as a small number of large super clusters emerge. This forges the formation of a continuous ethanol microphase, as the ethanol microstructure rapidly evolves toward its pure-liquid limit (as sketched in Figure 10c). A growing ethanol continuum besieges a dwindling number of benzene molecules that become increasingly isolated. Localized benzene-rich regions, formed during stage 2, now gradually diminish. Increasing exposure of benzene to ethanol leads to less favorable interactions and increased volatility of benzene. Meanwhile, HB statistics have mostly converged and ethanol volatility does not change as much.

Representative direct molecular images from the GEMC simulation are shown in Figure 11. At the lowest concentration

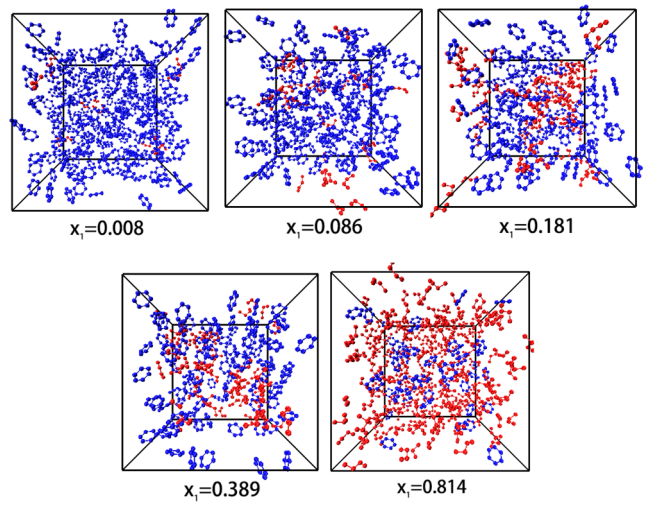

Figure 11. Representative images of instantaneous molecular configurations in the liquid cell: (red) ethanol; (blue) benzene. The first three cases ($x_1 = 0.008$, 0.086, and 0.181) are in stage 1, the fourth ($x_1 = 0.389$) is in stage 2, and the last ($x_1 = 0.814$) is in stage 3.

$x_1 = 0.008$, ethanol molecules are isolated from one another. Clusters of ethanol molecules are found at $x_1 = 0.086$, which become both denser and larger at $x_1 = 0.181$. In stage 2 ($x_1 = 0.389$), ethanol- and benzene-rich regions are clearly identifiable. At the highest concentration shown ($x_1 = 0.814$), benzene molecules are nearly all isolated and surrounded by an ethanol continuum.

We expect this molecular mechanism to be generalizable to similar positive azeotropes where one component is significantly more polar than the other and has a strong tendency to self-associate, such as methanol/benzene or even chloroform/methanol. However, for positive azeotropes where both components are polar and strong association can occur within both species as well as between species, such as ethanol/water, patterns of molecular arrangement at different composition

https://dx.doi.org/10.1021/acs.jpcb.9b12013
J. Phys. Chem. B 2020, 124, 3371−3386

levels are expected to be different. Furthermore, for negative azeotropes, such as water/formic acid or acetone/chloroform, cross-species association in the mixture might be stronger than that between molecules of the same species and thus a different mechanism is also expected. Our most significant contribution is the demonstration of a new approach for azeotrope study, which focuses on thermodynamic properties and liquid microstructure variations over a wider composition range than the azeotrope point. Specific molecular mechanisms arising from this approach would differ between different types of azeotropes. Its application to broader systems is still needed. Finally, we note that the thermodynamic criterion discussed in section 3.2 is generally applicable to all azeotrope systems, except that for negative azeotropes, the two inequalities in eq 13 must be swapped between the $x_1 < x_1^{aze}$ and $x_1 > x_1^{aze}$ cases.

4. CONCLUSIONS

In this study, GEMC is used to investigate the VLE behavior of the ethanol/benzene mixture over the entire composition range. The simulation results reproduce the experimental phase diagram, including an accurate prediction of the azeotrope point. We emphasize that the necessary and sufficient condition for the occurrence of azeotrope is the changing order of relative volatility between the two components. For the ethanol/benzene system studied here, which has a positive azeotrope, ethanol is more volatile than benzene at $x_1 < x_1^{aze}$ whereas benzene becomes more volatile at $x_1 > x_1^{aze}$. Molecular understanding of azeotrope formation thus requires the explanation of the changing volatility of the two components over a much wider composition range than the azeotrope point itself.

A thermodynamic criterion has thus been derived on the basis of the comparison of partial excess Gibbs energy between the two components (eqs 11 and 13). Application to the ethanol/benzene system simulated in this study shows that there are at least two stages of different dominant mechanisms for the changing relative volatility. At lower ethanol mole fraction x_1, volatility of ethanol decreases significantly with increasing x_1 while that of benzene stays nearly constant. At higher x_1, ethanol volatility no longer changes but benzene becomes increasingly volatile. Analysis of molecular energetics shows that these free energy variations are dominated by energetic interactions, especially self-interactions between molecules of the same species. As x_1 increases, at lower x_1, each ethanol molecule feels stronger total attraction from other ethanol molecules in the mixture, whereas at higher x_1, each benzene molecule feels less total attraction from other benzene molecules.

Molecular energetics is studied through the microscopic liquid structure, using RDF, KBI, and HB analysis. It is concluded that, with increasing x_1, there are three stages of different molecular organization patterns. HBs start to form at very low x_1, and in stage 1, ethanol molecules quickly cluster in the ocean of benzene. Cluster size and density increase with increasing x_1. In stage 2, which for the conditions studied here starts at $x_1 \approx 0.2$, ethanol clusters further aggregate and cause microscopic segregation between ethanol- and benzene-rich regions. In stage 3, which starts at $x_1 \approx 0.5$, further increasing x_1 results in the coalition of smaller clusters into larger ones and ethanol forms a continuous phase, leaving benzene molecules increasingly isolated. Since stage 1 sees the most increase in the number of HBs per molecule, it is where ethanol molecules are increasingly attracted in the liquid phase and become less volatile. At higher x_1, HB increments are much slower, which explains the later plateauing of ethanol volatility. Meanwhile, throughout stages 1 and 2, benzene molecules are surrounded mostly by other benzene molecules. This only changes in stage 3, where ethanol clusters are large and dense enough to cause the ghettoization of benzene and its increasing isolation. Higher exposure to ethanol causes its raised volatility in this regime.

This is to our knowledge the first full molecular mechanism for the existence of an azeotrope considering the variations in thermodynamic properties over the whole composition range. It is expected to be generalizable to other systems with positive azeotropes between a polar and nonpolar species.

A. COHESIVE ENERGY AND BINDING ENERGY

In this Appendix, we give detailed mathematical definitions of cohesive and binding energies and discuss the conceptual relationships between energetic quantities.

A.1. Cohesive Energy. In a binary mixture, the molar cohesive energy E^{coh} is calculated according to its definition

$$E^{coh} \equiv x_1 E_1^{iso} + x_2 E_2^{iso} - E^{bulk} \tag{25}$$

where E^{bulk} is the molar potential energy of the liquid mixture and

$$E_1^{iso} = \mathcal{N}_{AV}\langle e_1^{iso}\rangle \tag{26}$$

$$E_2^{iso} = \mathcal{N}_{AV}\langle e_2^{iso}\rangle \tag{27}$$

are the potential energy of infinitely separated molecules of component 1 and 2, respectively (scaled to the basis of 1 mol of the species), when each molecule is isolated in a vacuum.[83] In eq 26 and eq 27, e_1^{iso} and e_2^{iso} are the energy of one single molecule placed in a vacuum, $\mathcal{N}_{Av}$ is the Avogadro constant, and $\langle\cdot\rangle$ indicates the ensemble average. The potential energy E^{bulk} is the summation of bonded (bond stretching, bending, and torsion potentials; see Table 2) and nonbonded or pairwise (Lennard-Jones and Coulombic potentials) interactions, and the latter is further divided into intra- and intermolecular components:

$$E^{bulk} = E^{bonded} + E^{nonbonded} = E^{bonded} + E^{intra} + E^{inter} \tag{28}$$

where all these terms are on the basis of 1 mol of the mixture. Between the bulk liquid and isolated state, the energy contained within each molecule changes very little, i.e.,

$$E^{bonded} + E^{intra} \approx x_1 E_1^{iso} + x_2 E_2^{iso} \tag{29}$$

which, combined with eqs 25 and 28, leads to eq 18. The cohesive energy is thus directly related to the total intermolecular pairwise interactions in the mixture. The latter is the summation of the interactions between all individual molecular pairs

$$E^{inter} = \frac{1}{2}\sum_{\iota=1}^{n_1}\sum_{\substack{\kappa=1\\ \kappa\neq\iota}}^{n_1} e_{11}(\iota,\kappa) + \frac{1}{2}\sum_{\iota=1}^{n_2}\sum_{\substack{\kappa=1\\ \kappa\neq\iota}}^{n_2} e_{22}(\iota,\kappa) + \sum_{\iota=1}^{n_1}\sum_{\kappa=1}^{n_2} e_{12}(\iota,\kappa) \tag{30}$$

where ι and κ are indices for molecules, n_i is the number of molecules of type i in 1 mol of the mixture, and $e_{ij}(\iota,\kappa)$ is the interaction potential between molecule ι of type i and molecule

https://dx.doi.org/10.1021/acs.jpcb.9b12013
J. Phys. Chem. B 2020, 124, 3371−3386

κ of type j. The first two terms are interactions between molecules of the same type and a factor of 1/2 is needed because each pair is counted twice in the double-loop summation.

A.2. Binding Energy. To strip one component-1 molecule, indexed by ι, away from the mixture to infinite distance, its pairwise intermolecular interactions with all other molecules, which remain in place, must be broken. The energy required is

$$e_1^{\text{bind}}(\iota) = e_{11}^{\text{bind}} + e_{12}^{\text{bind}} \approx -\left(\sum_{\substack{\kappa=1 \\ \kappa\neq\iota}}^{n_1} e_{11}(\iota,\kappa) + \sum_{\kappa=1}^{n_2} e_{12}(\iota,\kappa) \right) \tag{31}$$

(the approximate sign, $\approx$, again would become an equal sign, =, if we assume no change in the bonded and intramolecular nonbonded interactions as the molecule leaves the liquid phase). The two summations on the right-hand side correspond to contributions from self-interaction (with other molecules of component 1) e_{11}^{bind} and cross-interaction (with molecules of component 2) e_{12}^{bind}, respectively. Scaling this energy, which is for the removal of a single molecule, to the per mole (of component 1) basis, we obtain the molar binding energy of component 1

$$\begin{aligned} E_1^{\text{bind}} &= E_{11}^{\text{bind}} + E_{12}^{\text{bind}} \\ &\approx -\frac{1}{x_1} \sum_{\iota=1}^{n_1} \left(\sum_{\substack{\kappa=1 \\ \kappa\neq\iota}}^{n_1} e_{11}(\iota,\kappa) + \sum_{\kappa=1}^{n_2} e_{12}(\iota,\kappa) \right) \end{aligned} \tag{32}$$

which is again decomposed into self- and cross-interaction terms E_{11}^{bind} and E_{12}^{bind}. The molar binding energy of component 2

$$\begin{aligned} E_2^{\text{bind}} &= E_{22}^{\text{bind}} + E_{21}^{\text{bind}} \\ &\approx -\frac{1}{x_2} \sum_{\kappa=1}^{n_2} \left(\sum_{\substack{\iota=1 \\ \iota\neq\kappa}}^{n_2} e_{22}(\iota,\kappa) + \sum_{\iota=1}^{n_1} e_{12}(\iota,\kappa) \right) \end{aligned} \tag{33}$$

is likewise defined.

Calculation. E_1^{bind} is calculated by first carving out all component-2 molecules from the simulation cell while leaving component-1 molecules frozen in place. The cohesive energy of the resulting cell contains contributions from 1 to 1 self-interactions only, from which E_{11}^{bind} can be calculated. Likewise, E_{22}^{bind} is calculated by removing all component-1 molecules in the cell. The cross-terms, i.e., E_{12}^{bind} or E_{21}^{bind}, can then be calculated from the cohesive energy of the original mixture cell as well as the above results by invoking eq 18 and 30.

Comparison with Partial Molar Energy. It is natural to draw a connection between molar binding energy and partial molar energy, both of which appear to describe marginal energy changes associated with adding or removing molecules. These two quantities are conceptually related but not the same. Discussion here thus attempts to make a distinction between them. Partial molecular energy measures the marginal changes in energy caused by the addition of a differentially small amount of one component, also scaled to the basis of 1 mol of the species concerned. In our definition, $-E_1^{\text{bind}}$ (or $-E_2^{\text{bind}}$; minus sign because binding energy is defined on the basis of the removal rather than addition of the molecules) clearly has a similar physical meaning, but it misses two important components in partial molar energy: (1) the intramolecular energy components (bonded and nonbonded) and (2), more importantly, energy changes caused by the reorganization of the remaining molecules after the addition or removal of the selected molecule. It is, however, much more straightforward to compute, which only requires the system configuration. In comparison, computation of partial properties typically requires either particle insertion with ensemble sampling or numerical differentiation over different composition levels, which remains a nontrivial challenge especially for polyatomic molecular fluids.[84,85]

Relationship with Cohesive Energy. Combining eqs 18, 30, 32, and 33, we now get

$$E^{\text{inter}} \approx -E^{\text{coh}} = -\frac{1}{2}(x_1 E_1^{\text{bind}} + x_2 E_2^{\text{bind}}) \tag{34}$$

(the second relation is = because the errors due to the slightly different bonded and intramolecular nonbonded interactions between the isolated and condensed states of individual molecules are contained in both eq 18 and eqs 32 and 33, allowing them to cancel one another). Equation 34 is reminiscent of the summability relation between the mixture molar energy and component partial molar energies

$$U = x_1 \bar{U}_1 + x_2 \bar{U}_2 \tag{35}$$

and, therefore, $-(1/2)E_1^{\text{bind}}$ and $-(1/2)E_2^{\text{bind}}$ can be similarly interpreted as the contributions to the liquid-phase intermolecular interactions E^{inter} from individual components. The factor of 1/2 in eq 34 is because the intermolecular interaction between each pair of molecules is counted twice in E_1^{bind} and E_2^{bind} combined.

AUTHOR INFORMATION

Corresponding Authors

Xin Gao − *School of Chemical Engineering and Technology, National Engineering Research Center of Distillation Technology, and Collaborative Innovation Center of Chemical Science and Engineering (Tianjin), Tianjin University, Tianjin 300072, China;* orcid.org/0000-0002-0739-8440; Email: gaoxin@tju.edu.cn

Li Xi − *Department of Chemical Engineering, McMaster Universtiy, Hamilton, Ontario L8S 4L7, Canada;* orcid.org/0000-0002-1509-1350; Email: xili@mcmaster.ca; http://www.xiresearch.org

Authors

Dongyang Li − *School of Chemical Engineering and Technology, National Engineering Research Center of Distillation Technology, and Collaborative Innovation Center of Chemical Science and Engineering (Tianjin), Tianjin University, Tianjin 300072, China; Department of Chemical Engineering, McMaster Universtiy, Hamilton, Ontario L8S 4L7, Canada*

Ziqi Gao − *Department of Chemical Engineering, McMaster Universtiy, Hamilton, Ontario L8S 4L7, Canada*

Naveen Kumar Vasudevan − *Department of Chemical Engineering, McMaster Universtiy, Hamilton, Ontario L8S 4L7, Canada*

Hong Li − *School of Chemical Engineering and Technology, National Engineering Research Center of Distillation Technology, and Collaborative Innovation Center of Chemical Science and Engineering (Tianjin), Tianjin University, Tianjin 300072, China*

https://dx.doi.org/10.1021/acs.jpcb.9b12013
J. Phys. Chem. B 2020, 124, 3371−3386

Xingang Li − *School of Chemical Engineering and Technology, National Engineering Research Center of Distillation Technology, and Collaborative Innovation Center of Chemical Science and Engineering (Tianjin), Tianjin University, Tianjin 300072, China*

Complete contact information is available at: https://pubs.acs.org/10.1021/acs.jpcb.9b12013

Notes

The authors declare no competing financial interest.

■ ACKNOWLEDGMENTS

The authors acknowledge the financial support by the Natural Sciences and Engineering Research Council (NSERC) of Canada (RGPIN-4903-2014) and the National Natural Science Foundation of China (NFSC; No. 21878219). We also acknowledge Compute/Calcul Canada for its allocation of computing resource. D.L. thanks the China Scholarship Council (CSC) for supporting his doctoral study at McMaster University (No. 201500090106). This work is also made possible by the facilities of the Shared Hierarchical Academic Research Computing Network (SHARCNET: www.sharcnet.ca).

■ REFERENCES

(1) Gmehling, J.; Onken, U.; Behrens, D.; Eckermann, R. *Vapor-liquid equilibrium data collection: Aqueous-organic systems*; Dechema: Frankfurt, Germany, 1977; Vol. *1*, Part 1.

(2) Gmehling, J.; Menke, J.; Krafczyk, J.; Fischer, K.; Pereira Nunes, S.; Peinemann, K. *Azeotropic data*; Wiley Online Library, 1994.

(3) Gmehling, J.; Möllmann, C. Synthesis of distillation processes using thermodynamic models and the dortmund data bank. *Ind. Eng. Chem. Res.* **1998**, *37* (8), 3112−3123.

(4) Michelsen, M. L A method for incorporating excess gibbs energy models in equations of state. *Fluid Phase Equilib.* **1990**, *60* (1−2), 47−58.

(5) Kontogeorgis, G. M.; Folas, G. K. Thermodynamic models for industrial applications. *From Classical and Advanced Mixing Rules to Association Theories*; Wiley, 2010.

(6) Soave, G. Equilibrium constants from a modified redlich-kwong equation of state. *Chem. Eng. Sci.* **1972**, *27* (6), 1197−1203.

(7) Peng, D.-Y.; Robinson, D. B. A new two-constant equation of state. *Ind. Eng. Chem. Fundam.* **1976**, *15* (1), 59−64.

(8) Magnussen, T.; Rasmussen, P.; Fredenslund, A. Unifac parameter table for prediction of liquid-liquid equilibriums. *Ind. Eng. Chem. Process Des. Dev.* **1981**, *20* (2), 331−339.

(9) Hansen, H. K.; Rasmussen, P.; Fredenslund, A.; Schiller, M.; Gmehling, J. Vapor-liquid equilibria by unifac group contribution. 5. revision and extension. *Ind. Eng. Chem. Res.* **1991**, *30* (10), 2352−2355.

(10) Barr-David, F.; Dodge, B. F. Vapor-liquid equilibrium at high pressures. the systems ethanol-water and 2-propanol-water. *J. Chem. Eng. Data* **1959**, *4* (2), 107−121.

(11) Kurihara, K.; Nakamichi, M.; Kojima, K. Isobaric vapor-liquid equilibria for methanol+ ethanol+ water and the three constituent binary systems. *J. Chem. Eng. Data* **1993**, *38* (3), 446−449.

(12) Hellwig, L. R.; van Winkle, M. Vapor-liquid equilibria for ethyl alcohol binary systems. *Ind. Eng. Chem.* **1953**, *45* (3), 624−629.

(13) Gmehling, J.; Menke, J.; Krafczyk, J.; Fischer, K. A data bank for azeotropic data-status and applications. *Fluid Phase Equilib.* **1995**, *103* (1), 51−76.

(14) Maier, R. W.; Brennecke, J. F.; Stadtherr, M. A. Reliable computation of homogeneous azeotropes. *AIChE J.* **1998**, *44* (8), 1745−1755.

(15) Calvar, N.; González, B.; Gómez, E.; Domínguez, A. Study of the behaviour of the azeotropic mixture ethanol-water with imidazolium-based ionic liquids. *Fluid Phase Equilib.* **2007**, *259* (1), 51−56.

(16) Onori, G. Structural properties of aqueous mixtures of monohydric alcohols from near-infrared absorption spectra. *Chem. Phys. Lett.* **1989**, *154* (3), 213−216.

(17) Williams, R. W.; Cheh, J. L.; Lowrey, A. H.; Weir, A. F. Effects of hydration on scale factors for ab initio force constants. 9. methanol. *J. Phys. Chem.* **1995**, *99* (15), 5299−5307.

(18) Wakisaka, A.; Abdoul-Carime, H.; Yamamoto, Y.; Kiyozumi, Y. Non-ideality of binary mixtures water-methanol and water-acetonitrile from the viewpoint of clustering structure. *J. Chem. Soc., Faraday Trans.* **1998**, *94* (3), 369−374.

(19) Vaz, P. D.; Nolasco, M. M.; Gil, F. P. S. C.; Ribeiro-Claro, P. J. A.; Tomkinson, J. Hydrogen-bond dynamics of c-h-o interactions: The chloroform-acetone case. *Chem. - Eur. J.* **2010**, *16* (30), 9010−9017.

(20) Huggins, C. M.; Pimentel, G. C.; Shoolery, J. N. Proton magnetic resonance studies of chloroform in solution: evidence for hydrogen bonding. *J. Chem. Phys.* **1955**, *23* (7), 1244−1247.

(21) Choi, K.; Tedder, D. W. Molecular interactions in chloroform-diluent mixtures. *AIChE J.* **1997**, *43* (1), 196−211.

(22) Matsumoto, M.; Nishi, N.; Furusawa, T.; Saita, M.; Takamuku, T.; Yamagami, M.; Yamaguchi, T. Structure of clusters in ethanol-water binary solutions studied by mass spectrometry and x-ray diffraction. *Bull. Chem. Soc. Jpn.* **1995**, *68* (7), 1775−1783.

(23) Jalilian, M. R.; Alibabaei, L. Spectra and structure of binary azeotropes: I. acetone-chloroform. *Spectrochim. Acta, Part A* **2005**, *62* (1−3), 322−325.

(24) Perova, T. S.; Christensen, D. H.; Nielsen, O. F. Low-frequency raman and far-infrared spectra of acetone/chloroform mixtures. *Vib. Spectrosc.* **1997**, *15* (1), 61−67.

(25) Jalilian, M. R. Spectra and structure of binary azeotropes: Ii. acetone-n-pentane. *Spectrochim. Acta, Part A* **2007**, *66* (1), 91−93.

(26) Jalilian, M. R.; Tayyari, S. F. Spectra and structure of binary azeotropes vi-benzene-methanol. *Spectrochim. Acta, Part A* **2009**, *73* (5), 828−832.

(27) Jalilian, M. R. Spectra and structure of binary azeotropes: Iv. acetone-cyclohexane. *Spectrochim. Acta, Part A* **2008**, *69* (3), 812−815.

(28) Jalilian, M. R.; Zahedi-Tabrizi, M. Spectra and structure of binary azeotropes v-acetone-cyclopentane. *Spectrochim. Acta, Part A* **2008**, *69* (1), 278−281.

(29) Ripoll, J. D.; Mejía, S. M.; Mills, M. J. L.; Villa, A. L. Understanding the azeotropic diethyl carbonate-water mixture by structural and energetic characterization of dec$(h_2o)_n$ heteroclusters. *J. Mol. Model.* **2015**, *21* (4), 93.

(30) Matisz, G.; Kelterer, A.; Fabian, W. M. F.; Kunsági-Máté, S. Coordination of methanol clusters to benzene: a computational study. *J. Phys. Chem. A* **2011**, *115* (38), 10556−10564.

(31) Waluyo, B.; Wardana, I. N. G.; Yuliati, L.; Sasongko, M. N. The role of molecule cluster on the azeotrope and boiling points of isooctane-ethanol blend. *Fuel* **2018**, *215*, 178−186.

(32) Baburao, B.; Visco, D. P.; Albu, T. V. Association patterns in $(hf)_m$ $(h_2o)_n$ (m + n= 2−8) clusters. *J. Phys. Chem. A* **2007**, *111* (32), 7940−7956.

(33) Mejía, S. M.; Espinal, J. F.; Mondragón, F. Cooperative effects on the structure and stability of $(ethanol)_3$-water, $(methanol)_3$-water heterotetramers and $(ethanol)_4$, $(methanol)_4$ tetramers. *J. Mol. Struct.: THEOCHEM* **2009**, *901* (1−3), 186−193.

(34) Shephard, J. J.; Callear, S. K.; Imberti, S.; Evans, J. S. O.; Salzmann, C. G. Microstructures of negative and positive azeotropes. *Phys. Chem. Chem. Phys.* **2016**, *18* (28), 19227−19235.

(35) Soper, A. K. Empirical potential monte carlo simulation of fluid structure. *Chem. Phys.* **1996**, *202* (2−3), 295−306.

(36) Soper, A. K. Partial structure factors from disordered materials diffraction data: An approach using empirical potential structure refinement. *Phys. Rev. B: Condens. Matter Mater. Phys.* **2005**, *72* (10), 104204.

(37) Wakisaka, A.; Matsuura, K. Microheterogeneity of ethanol-water binary mixtures observed at the cluster level. *J. Mol. Liq.* **2006**, *129* (1−2), 25−32.
(38) Wakisaka, A.; Matsuura, K.; Uranaga, M.; Sekimoto, T.; Takahashi, M. Azeotropy of alcohol-water mixtures from the viewpoint of cluster-level structures. *J. Mol. Liq.* **2011**, *160* (2), 103−108.
(39) Wakisaka, A.; Iwakami, T. Molecular clustering inherent in the liquid state: Effect of relativity in intermolecular interaction energy. *J. Mol. Liq.* **2014**, *189*, 44−51.
(40) Panagiotopoulos, A. Z. Direct determination of phase coexistence properties of fluids by monte carlo simulation in a new ensemble. *Mol. Phys.* **1987**, *61* (4), 813−826.
(41) Panagiotopoulos, A. Z.; Quirke, N.; Stapleton, M.; Tildesley, D. J. Phase equilibria by simulation in the gibbs ensemble: alternative derivation, generalization and application to mixture and membrane equilibria. *Mol. Phys.* **1988**, *63* (4), 527−545.
(42) Frenkel, D.; Smit, B. *Understanding Molecular Simulation: from Algorithms to Applications*, 2nd ed.; Academic Press: London, 2002.
(43) Scalise, O. H.; Gianotti, R. D.; Zarragoicoechea, G. J.; Rodriguez, A. E. Azeotropic states in the co_2-c_2h_6 mixture from the hard sphere lennard-jones quadrupolar molecular model. *J. Chem. Phys.* **1989**, *91* (7), 4273−4277.
(44) Kofke, D. A. Direct evaluation of phase coexistence by molecular simulation via integration along the saturation line. *J. Chem. Phys.* **1993**, *98* (5), 4149−4162.
(45) Pandit, S. P.; Kofke, D. A. Evaluation of a locus of azeotropes by molecular simulation. *AIChE J.* **1999**, *45* (10), 2237−2244.
(46) Panagiotopoulos, A. Z. Molecular simulation of phase equilibria. In *Supercritical Fluids*; Kiran, E., Levelt Sengers, J. M. H., Eds.; Springer, 1994; pp 411−437.
(47) Lamm, M. H.; Hall, C. K. Molecular simulation of complete phase diagrams for binary mixtures. *AIChE J.* **2001**, *47* (7), 1664−1675.
(48) Bruce, A. D.; Wilding, N. B. Scaling fields and universality of the liquid-gas critical point. *Phys. Rev. Lett.* **1992**, *68* (2), 193.
(49) Panagiotopoulos, A. Z. Monte carlo methods for phase equilibria of fluids. *J. Phys.: Condens. Matter* **2000**, *12* (3), R25.
(50) Ferrando, N.; Lachet, V.; Boutin, A. Monte carlo simulations of mixtures involving ketones and aldehydes by a direct bubble pressure calculation. *J. Phys. Chem. B* **2010**, *114* (26), 8680−8688.
(51) Hadj-Kali, M. K.; Gerbaud, V.; Joulia, X. Azeotrope prediction by monte carlo molecular simulation. *Chem. Eng. Commun.* **2012**, *199* (5), 673−688.
(52) Kamath, G.; Georgiev, G.; Potoff, J. J. Molecular modeling of phase behavior and microstructure of acetone-chloroform-methanol binary mixtures. *J. Phys. Chem. B* **2005**, *109* (41), 19463−19473.
(53) Lísal, M.; Smith, W. R.; Nezbeda, I. Accurate vapour-liquid equilibrium calculations for complex systems using the reaction gibbs ensemble monte carlo simulation method. *Fluid Phase Equilib.* **2001**, *181* (1−2), 127−146.
(54) Chen, B.; Potoff, F. J.; Siepmann, J. I. Monte carlo calculations for alcohols and their mixtures with alkanes. transferable potentials for phase equilibria. 5. united-atom description of primary, secondary, and tertiary alcohols. *J. Phys. Chem. B* **2001**, *105* (15), 3093−3104.
(55) Wick, C. D.; Stubbs, J. M.; Rai, N.; Siepmann, J. I. Transferable potentials for phase equilibria. 7. primary, secondary, and tertiary amines, nitroalkanes and nitrobenzene, nitriles, amides, pyridine, and pyrimidine. *J. Phys. Chem. B* **2005**, *109* (40), 18974−18982.
(56) Sum, A. K.; Sandler, S. I.; Bukowski, R.; Szalewicz, K. Prediction of the phase behavior of acetonitrile and methanol with ab initio pair potentials. ii. the mixture. *J. Chem. Phys.* **2002**, *116* (17), 7637−7644.
(57) Li, H.; Zhang, Ji; Li, D.; Li, X.; Gao, X. Monte carlo simulations of vapour-liquid phase equilibrium and microstructure for the system containing azeotropes. *Mol. Simul.* **2017**, *43* (13−16), 1125−1133.
(58) Martin, M. G.; Siepmann, J. I. Transferable potentials for phase equilibria. 1. united-atom description of n-alkanes. *J. Phys. Chem. B* **1998**, *102* (14), 2569−2577.
(59) Martin, M. G. Mcccs towhee: a tool for monte carlo molecular simulation. *Mol. Simul.* **2013**, *39* (14−15), 1212−1222.
(60) Lorentz, H. A. Ueber die anwendung des satzes vom virial in der kinetischen theorie der gase. *Ann. Phys.* **1881**, *248* (1), 127−136.
(61) Berthelot, D. Sur le mélange des gaz. *Compt. Rend.* **1898**, *126*, 1703−1706.
(62) Allen, M. P.; Tildesley, D. J. *Computer simulation of liquids*; Clarendon Press: Oxford, U.K., 1987.
(63) Wood, W. W.; Parker, F. R. Monte carlo equation of state of molecules interacting with the lennard-jones potential. i. a super-critical isotherm at about twice the critical temperature. *J. Chem. Phys.* **1957**, *27* (3), 720−733.
(64) Wick, C. D.; Martin, M. G.; Siepmann, J .I. Transferable potentials for phase equilibria. 4. united-atom description of linear and branched alkenes and alkylbenzenes. *J. Phys. Chem. B* **2000**, *104* (33), 8008−8016.
(65) Martin, M G.; Siepmann, J. I. Novel configurational-bias monte carlo method for branched molecules. transferable potentials for phase equilibria. 2. united-atom description of branched alkanes. *J. Phys. Chem. B* **1999**, *103* (21), 4508−4517.
(66) Potoff, J. J.; Siepmann, J. I. Vapor-liquid equilibria of mixtures containing alkanes, carbon dioxide, and nitrogen. *AIChE J.* **2001**, *47* (7), 1676−1682.
(67) Petersen, H.; Flyvbjerg, H. Error estimates in molecular dynamics simulations. *J. Chem. Phys.* **1989**, *91*, 461−467.
(68) Stubbs, J. M.; Potoff, J. J.; Siepmann, J. I. Transferable potentials for phase equilibria. 6. united-atom description for ethers, glycols, ketones, and aldehydes. *J. Phys. Chem. B* **2004**, *108* (45), 17596−17605.
(69) Lubna, N.; Kamath, G.; Potoff, J. J.; Rai, N.; Siepmann, J. I. Transferable potentials for phase equilibria. 8. united-atom description for thiols, sulfides, disulfides, and thiophene. *J. Phys. Chem. B* **2005**, *109* (50), 24100−24107.
(70) Rai, N.; Siepmann, J. I. Transferable potentials for phase equilibria. 9. explicit hydrogen description of benzene and five-membered and six-membered heterocyclic aromatic compounds. *J. Phys. Chem. B* **2007**, *111* (36), 10790−10799.
(71) Gao, X.; Li, X.; Zhang, J.; Sun, J.; Li, H. Influence of a microwave irradiation field on vapor-liquid equilibrium. *Chem. Eng. Sci.* **2013**, *90*, 213−220.
(72) Smith, J. M. *Introduction to chemical engineering thermodynamics*; McGraw Hill, 1950.
(73) Müller-Plathe, F.; van Gunsteren, W. F. Solvation of poly (vinyl alcohol) in water, ethanol and an equimolar water-ethanol mixture: structure and dynamics studied by molecular dynamics simulation. *Polymer* **1997**, *38* (9), 2259−2268.
(74) Zhang, C.; Yang, X. Molecular dynamics simulation of ethanol/water mixtures for structure and diffusion properties. *Fluid Phase Equilib.* **2005**, *231* (1), 1−10.
(75) Kirkwood, J. G.; Buff, F. P. The statistical mechanical theory of solutions. I. *J. Chem. Phys.* **1951**, *19*, 774−777.
(76) Haughney, M.; Ferrario, M.; McDonald, I. R. Molecular-dynamics simulation of liquid methanol. *J. Phys. Chem.* **1987**, *91*, 4934−4940.
(77) Padró, J. A.; Saiz, L.; Guàrdia, E. Hydrogen bonding in liquid alcohols: A computer simulation study. *J. Mol. Struct.* **1997**, *416*, 243−248.
(78) Luzar, A.; Chandler, D. Effect of environment on hydrogen bond dynamics in liquid water. *Phys. Rev. Lett.* **1996**, *76* (6), 928.
(79) Saiz, L.; Padro, J. A.; Guardia, E. Dynamics and hydrogen bonding in liquid ethanol. *Mol. Phys.* **1999**, *97*, 897−905.
(80) Noskov, S. Yu.; Lamoureux, G.; Roux, B. Molecular dynamics study of hydration in ethanol-water mixtures using a polarizable force field. *J. Phys. Chem. B* **2005**, *109*, 6705−6713.
(81) Vrhovšek, A.; Gereben, O.; Jamnik, A.; Pusztai, L. Hydrogen bonding and molecular aggregates in liquid methanol, ethanol, and 1-propanol. *J. Phys. Chem. B* **2011**, *115*, 13473−13488.
(82) Ghoufi, A.; Artzner, F.; Malfreyt, P. Physical Properties and Hydrogen-Bonding Network of Water-Ethanol Mixtures from

https://dx.doi.org/10.1021/acs.jpcb.9b12013
J. Phys. Chem. B 2020, 124, 3371−3386

Molecular Dynamics Simulations. *J. Phys. Chem. B* **2016**, *120*, 793−802.
(83) Li, D.; Panchal, K.; Mafi, R.; Xi, L. An atomistic evaluation of the compatibility and plasticization efficacy of phthalates in poly (vinyl chloride). *Macromolecules* **2018**, *51* (18), 6997−7012.
(84) Sindzingre, P.; Massobrio, C.; Ciccotti, G.; Frenkel, D. Calculation of partial enthalpies of an argon-krypton mixture by NPT molecular dynamics. *Chem. Phys.* **1989**, *129*, 213−224.
(85) Rahbari, A.; Hens, R.; Nikolaidis, I. K.; Poursaeidesfahani, A.; Ramdin, M.; Economou, I. G.; Moultos, O. A.; Dubbeldam, D.; Vlugt, T. J. H. Computation of partial molar properties using continuous fractional component Monte Carlo. *Mol. Phys.* **2018**, *116*, 3331−3344.

https://dx.doi.org/10.1021/acs.jpcb.9b12013
J. Phys. Chem. B 2020, 124, 3371−3386